Ionospheric response over Brazil to the August 2018 geomagnetic storm as probed by CSES-01 and Swarm satellites and by local ground-based observations

Spogli L.[1,2], Sabbagh D.[1], Regi M.[1], Cesaroni C.[1], Perrone L.[1], Alfonsi L.[1], Di Mauro D.[1], Lepidi S.[1], Campuzano S.A.[1,*], Marchetti D.[1,3], De Santis A.[1,4], Malagnini A.[1], Scotto C[1], Cianchini G.[1], Xuhui Shen[6], Piscini A.[1], Ippolito A.[5]

[1]Istituto Nazionale di Geofisica e Vulcanologia, Rome, Italy

[2]SpacEarth Technology, Rome, Italy

[3]Nanjing University of Information, Science and Technology, Nanjing, China

[4]University "Gabriele D'Annunzio", Chieti, Italy

[5]Italian Space Agency, Rome, Italy

[6]Institute of Crustal Dynamics, China Earthquake Administration, Beijing, China

*now at Instituto de Geociencias IGEO - CSIC, Madrid, Spain.

Corresponding author: Luca Spogli (luca.spogli@ingv.it)

Key points

- A detailed analysis of the storm-triggered EEJ variations and the resulting ionospheric variability is provided.

- Counter-electrojet found during 25 August daytime even under PPEF event.

- Use of CSES-01 and Swarm A plasma density data in a multi-instrument context to depict EIA crest signatures at different altitudes.

Abstract

The geomagnetic storm occurred on 25 August 2018, i.e. during the minimum of solar cycle 24, is currently the strongest ever probed by the first China Seismo-Electromagnetic Satellite (CSES-01). By integrating the *in situ* measurements provided by CSES-01 (orbiting at altitude of 507 km) and by Swarm A satellite (orbiting at ca. 470 km) with ground-based observations (ionosondes, magnetometers and Global Navigation Satellite System receivers), we investigate the ionospheric response at low- and mid- latitudes over Brazil. Specifically, we investigate the electrodynamic disturbances driven by solar wind changes, by focusing on the disturbances driving modifications of the Equatorial Electrojet (EEJ). Our proposed multi-sensor technique analysis mainly highlights the variations in the topside and bottomside ionosphere, and the interplay between Prompt Penetrating Electric Fields and Disturbance Dynamo Electric Fields resulting in EEJ variations. Thanks to this approach and leveraging on the newly available CSES-01 data, we complement and extend what recently investigated in the Western South American sector, by highlighting the significant longitudinal differences, which mainly come from the occurrence of a daytime counter-EEJ during both 25 and 26 August at Brazilian longitudes and during part of 26 August only in the Peruvian sector. In addition, the increased thermospheric circulation driven by the storm has an impact on the EEJ during the recovery phase of the storm. The observations at the CSES-01/Swarm altitudes integrated with the ground-based observation recorded signatures of Equatorial Ionospheric Anomaly (EIA) crests formation and modification during daytime coupled with the positive ionospheric storm effects at mid-latitude.

1. **Introduction**

The geomagnetic storm occurred in late August 2018 was triggered by such a gradual eruption of a large filament with associated coronal mass ejection (CME) from a quiet solar region that automatic detection tools failed to trigger an alert [*Vanlommel*, 2018]. This was not the only surprise the storm brought with it, but also its strength, resulting into the third strongest geomagnetic storm of the 24th solar cycle, reaching a minimum SYMH of -205 nT (5-minutes resolution) on 26 August at 07:10 UT (corresponding to minimum Dst= -174 nT (1-hour resolution), maximum Kp=7+ (3-hours resolution)). For a detailed description of the eruption and propagation characteristics, the reader is referred to the works by *Chen et al.* [2019] and by *Piersanti et al.* [2020]. This is, to date, the most intense storm occurred during the lifetime of the

CSES-01 satellite [*Shen et al.*, 2018], launched in February 2018. The detailed response of all instruments onboard CSES-01 to the geomagnetic storm is reported in *Yang et al.* [2020]. In this work, we exploit the complementary information provided by the *in situ* measurements of the plasma density by CSES-01 and Swarm A [*Friis-Christensen et al.*, 2008] satellites, as they cover comparable local time (LT) sectors during August 2018 at slightly different altitudes in the topside ionosphere (as explained in Section 2). Our aim is to provide a detailed picture of the ionospheric response to the geomagnetic storm over Brazil, also by leveraging on a dense network of ground-based instruments, which includes Global Navigation Satellite System (GNSS) receivers, ionosondes and magnetometers. The ionosphere in the Brazilian sector is one of the most important natural laboratories to understand the low-latitude electrodynamics and its modification following the day-to-day variability and geomagnetic storms occurrence [see., e.g., *Venkatesh et al.*, 2015; *Muella et al.*, 2010, 2017; *Spogli et al.*, 2013]. There, the ionosphere is featured by the presence of Equatorial Ionospheric Anomaly (EIA). The EIA is a local daytime depletion of the F-layer plasma density at the magnetic equator associated with two density peaks north and south of the magnetic equator [*McDougall*, 1969]. The formation and intensity of the EIA is modulated by the Equatorial Electrojet (EEJ) through the **ExB** plasma drifting [*Rishbeth*, 1971; *Kelley*, 2009; *Fejer*, 2011; *Balan et al.*, 2018]. EEJ flows eastward during daytime in a band of about ±3° around the magnetic equator, mainly generated by the dynamo mechanism in the ionospheric E-region [*Akiyama et al.*, 2019 and references therein]. At Brazilian longitudes, a current flowing westward, called Counter Electrojet (CEJ), is also present during the morning and the afternoon [*Rastogi et al.*, 2007]. Climatologically, the intensity of the EEJ and the consequent morphology of the EIA crests are modulated by the season, the solar flux and the occurrence of migrating and non-migrating tides [*Fejer et al.*, 1991, 2005; *Cardoso et al.*, 2011; *Yamazaki & Maute*, 2017]. Under equinoctial and high solar activity conditions, the expected position of the southern crest of the EIA reaches the most poleward latitudinal sector, i.e. in the southern hemisphere up to -20° off magnetic equator [see, e.g., *Cesaroni et al.*, 2015; *Muella et al.*, 2017]. The storm here investigated occurs under low solar flux and during local winter time, which results in the minimum conditions of the EIA intensity. This state favors two features: (i) the lowest probability of formation of Equatorial Plasma Bubbles (EPBs), that may drive scintillation of trans-ionospheric signals [*Kintner et al.*, 2009]; (ii) the exposure of the southernmost areas of the Brazilian ionosphere to typical phenomena of the mid-latitude ionosphere. Despite the focus of our paper is on daytime

variations, we can anticipate that the storm was able to trigger just small EPBs over Brazil as neither L-band scintillation events nor significant increase of Rate of TEC changes above the 0.5 TECu/minute threshold are found. The area is also influenced by the proximity to the South Atlantic Magnetic Anomaly (SAMA), where the lowest values of the geomagnetic field intensity at the Earth's surface are recorded [see, e.g., *Abdu et al.*, 2005]. The particle precipitation from the inner radiation belt in the SAMA region and the changes of declination in the region result, among the various effects, into a strong longitudinal dependence of the EEJ features [*Batista et al.*, 1986] and the alteration of the production and recombination rates of the ionized species, mainly during geomagnetic storms [see., e.g., *Spogli et al.*, 2013].

Under harsh geomagnetic conditions, two mechanisms disturb the low-latitude electrodynamics: the Prompt Penetration Electric Fields (PPEFs) and the Disturbance Dynamo Electric Fields (DDEFs). PPEFs are injected from the Solar Wind (SW) into the Earth's magnetic field lines down to ionospheric altitudes [*Nishida*, 1968], mainly during suddenly southward B_z variations. PPEFs are ruled out by the relative balance between Region 1 (R1) and Region 2 (R2) Field-Aligned Currents (FACs), that leads to different shielding conditions during the storm development [*Abdu et al.*, 2009; *Wei et al.*, 2015; *Fejer et al.*, 2017]. DDEFs are mainly due to the polarization fields that are westward in the dayside and eastward in the nightside. DDEFs follow the enhanced energy and momentum deposition in the high-latitude ionosphere, due to enhanced Joule heating and to Ampère force which lead to storm-time neutral winds [*Blanc and Richmond*, 1980; *Fuller-Rowell et al.*, 2002; *Yamazaki & Maute*, 2017]. The effect of DDEFs is usually delayed of about 1 to 3 hours, has typical time scales of the order of hours, and can last up to 1–2 days after geomagnetic activity has subsided [*Scherliess & Fejer*, 1997; *Fejer*, 2017]. On the contrary, PPEFs effect lasts about 30 minutes to 2 hours [*Venkatesh* et al, 2017].

When the two effects superimpose, the interpretation of their relative role in the resulting ionospheric disturbances is not an easy task. In addition, thermosphere composition changes reach the low latitude through equatorward winds, likely contributing to the deviation from the regular behavior of the EEJ [*Mendillo*, 2006; *Prölss*, 1995; *Fejer et al.*, 2017; *Yamazaki & Maute*, 2017; *Soares et al.*, 2018].

The paper complements and extends what reported by *Astafyeva et al.* [2020], who investigated the storm development in the neighboring longitudinal Peruvian sector and only during 25 and 26

August. We anticipate that, as indicated by *Abdu et al.* [2005], significant longitudinal difference between the EEJ features in the Western and Eastern South America, is found on 25 August, during which a strong CEJ is found during daytime and under PPEF event in the East sector, while only a small depletion of the daytime EEJ is found in the West sector (as in Figure 2c of *Astafyeva et al.*, 2020).

Other novelties introduced in the paper are:

(i)   the first use of the CSES-01 plasma density data in a multi-instrument context that includes space borne and ground-based instruments, able to depict simultaneously the ionospheric signatures of the EEJ variability in the investigated period in the bottomside and topside ionosphere and in the ionosphere as a whole;

(ii)   the detailed picture of the ionospheric response over the Brazilian sector to the August 2018 storm, from pre-storm conditions (including the day of 24 August) to the late recovery phase (to 31 August).

The paper is structured as follows: Section 2 details the large number of data used in this analysis and the corresponding methods; Section 3 provides the results, that are summarized in Section 4, together with the conclusions.

2.   **Data and Methods**

To analyze the ionospheric response over Brazil, we emphasize the information retrieved in the topside ionosphere by the *in situ* measurements from Swarm A and CSES-01 satellites at their passages over the target region during the storm time. Such information is complemented by the use of a network of ground-based instruments, which are reported in Figure 1. They provide information, through GNSS receivers (blue circles), ionosondes (red squares), and fluxgate magnetometers (green triangles). In the figure, the orange thick line represents the position of the magnetic equator in August 2018, as determined by integrating Swarm and CSES-01 magnetic measurements by using the same approach reported in Section 2.2.2 of the paper by *Spogli et al.* [2016]. This can also be done because magnetic measurements from these two satellites have been demonstrated to agree [*Yang et al.*, 2019]. Orange thin lines represent the isoclines at $\pm 5°$ and $\pm 10°$, to indicate the expected geographic coverage of the low-latitude ionization peak under low

solar activity and winter conditions, i.e. under the weakest conditions of the **ExB** intensity [see, e.g., *Venkatesh et al.*, 2015]. The network covers the region which expands from the expected position of the northern crest of the EIA to southern mid-latitudes, assumed to be located poleward with respect to the isoclinic line at -10°.

For detailing the storm features and characterizing its effects at Brazilian latitudes and longitudes, the geospace conditions and the activity indices are also considered (described in Section 2.4). These include the retrieval of the Equatorial Electric Field (EEF) and the Joule heating J_h due to particle precipitation and dissipation process of ionospheric electric currents at auroral latitudes of both hemispheres, to speculate about the relative role of PPEF and DDEF.

Time interval is from 24 to 31 August 2018, covering from pre-storm conditions to the late recovery phase. In that period, the sunrise and sunset hours at 120 km over the equator at the Brazilian longitudes are 08:26 UT (05:26 LT) and 22:10 UT (19:10 LT), respectively.

We carefully investigated the possible presence of Solar Energetic Particles (SEP) and Solar Flare (SF) events which could produce ionospheric/geomagnetic disturbances, analyzing protons (>100 MeV) and X-rays fluxes from geosynchronous GOES 14 and 15 satellites. In particular, SF events are able to suddenly modify the ionospheric conductivity and the pre-flare ionospheric current system conditions, resulting in geomagnetic/ionospheric SF effects, particularly evident during X-class flare events [see., e.g., *Villante & Regi*, 2008]. The results of our investigation (not shown here) clearly indicate the absence of such events.

2.1. CSES-01 and Swarm data

The first China Seismo-Electromagnetic Satellite (CSES-01) [*Shen et al.*, 2018] flies in a sun-synchronous polar orbit (97.4° inclination) at an altitude of 507 km. We take into consideration the plasma density provided by the Langmuir Probe (LP) onboard CSES-01 which consists of two sensors (Sensor 1 and Sensor 2) and an electronics box collocated inside the main body of the satellite. The instrument is composed by a pair of spherical LPs of 5-cm and 1-cm diameter, respectively, installed at a side of the satellite (that is a cube of about 1.4 m in dimension). CSES-01 provides a total of five levels of data (RAW, Level 1, 2, 3 and 4) [*Shen* et al., 2018]. Level 1 is the raw data converted in the proper units in instruments reference system, Level 2 are Level 1

data are rotated in an Earth reference system and Level 3 and Level 4 provide an automatic data processing in relation to some specific target, like seismic events, to investigate which, CSES-01 has been conceived. Here we use Level 2 data, i.e. data with physical quantities in an Earth reference system, by concentrating on the electron density (N_e) sampled every 3 seconds in the area of interest (while over the seismic belt and China territory, plasma parameters are sampled every 1.5 seconds), together with orbit information of the satellite after coordinate system transformation and inversion of Level 1 data [*Yan et al.*, 2018].

The Swarm satellite mission [*Friis-Christensen et al.*, 2008] is a constellation of three satellites, called *Alpha* (A), *Bravo* (B) and *Charlie* (C), which follow quasi-Sun-synchronous near-polar orbits at different altitudes: Swarm A and C fly at around 460 km (in 2018) above the Earth's surface and Swarm B at higher altitude (around 510 km). On board these satellites, a number of payloads allow monitoring the Earth's magnetic field and the ionosphere. The state of the ionosphere is probed by a LP measuring the main plasma parameters, among which N_e is considered here. The Swarm LP is composed of two identical spheres, so called "high-gain" and "low-gain" probes, of 8-mm diameter located Earth-facing. Data used in this study are collected by the Swarm LP at a rate of 2 Hz, provided as Level 1b data in Common Data Format (CDF) and freely available in the ESA Swarm FTP and HTTP Server swarm-diss.eo.esa.int. The Swarm data are also available from VIRES web platform: http://vires.services.

When comparing plasma density from Swarm and CSES-01, some caveats must be taken into account, as calibration and validation of CSES-01 plasma data is still ongoing and not completely assessed. In the specific, the ratio between the N_e measurements from Swarm A/C and CSES-01 has been found to be extremely variable (from about 5 up to 100) and be dependent on the probed density range. In the case of lowest ratio, that is the one characterizing this study (see Section 3), differences are attributable to:

- different altitude (about 35% difference in values)
- effect of sheath around the Swarm sensor caused by its negative polarization (about 50%)
- underestimation of plasma potential in the calculation of the electronic density of CSES-01 (about 50%).

Such features significantly affect quantitative comparison between the two kinds of plasma density measurements, while the proposed analysis, aimed mainly at identifying signatures of the ionospheric modifications following the storm, is little affected, as reported in Section 3.

In addition, Swarm satellites data products include estimations of the Equatorial Electric Field (EEF) from geomagnetic field measurements as Swarm Level 2 product (https://earth.esa.int/web/guest/document-library/browse-document-library/-/asset_publisher/lDo6/content/swarm-level-2-equatorial-electric-field-eef-product-description). From the latitudinal magnetic profiles recorded by the onboard magnetometers, EEF is estimated by inverting the observed magnetic measurements. Moreover, neutral thermospheric density from precise orbit determination and accelerometer data (https://earth.esa.int/documents/10174/1514862/Swarm_L2_Product_Specification) are also taken into account for Swarm C (data for Swarm A and B are not available for now).

To study N_e (and EEF, in the case of Swarm), we select daytime tracks of Swarm A and CSES-01 covering the Brazilian region, whose time windows are reported in Table 1, together with the corresponding mean LT of the tracks. The timing refers to the latitudinal range between 10°N and 35°S. We let the reader notice that the mean geographic LT of Swarm A is 15:22 for 10 August (selected as reference day for quiet conditions) and, being the satellite in a quasi-Sun-synchronous orbit, it drifts between 14:40 and 14:03 from 24 to 31 August. Conversely, the LT of CSES-01 is fixed at 14:02, being in a Sun-synchronous orbit. Such tracks are particularly suitable to study the EIA crests, because they are expected to peak around 14:00 LT [*Xiong et al.*, 2013]. The corresponding night-time tracks of Swarm A have been investigated to look for EPBs formation at Low-Earth Orbit (LEO) altitudes, without resulting in any clear signature (not shown). In the remainder of the paper, we adopt the naming "LEO satellites" when we simultaneously refer to both Swarm A and CSES-01.

2.2. **Ground-based magnetic data**

The geomagnetic observatories Tatuoca (TTB) and Kourou (KOU) (green triangles in Figure 1) are used to characterize the magnetic response to the storm at ground. In particular, we used a dataset at a 1-minute time resolution retrieved from the INTERMAGNET website (https://www.intermagnet.org/). The original horizontal magnetic field variations, provided in the geographic reference frame (*X* and *Y*), are converted in the geomagnetic *H* (northward) and *D*

(eastward) ones. The stations have a latitudinal separation of few degrees (~6°), as reported in Table 2: the TTB observatory, situated very close to the dip equator, records magnetic field variations strongly influenced by the EEJ, while the KOU observatory, far enough from the dip equator, does not [*Morschhauser et al.*, 2017]. This particular configuration allows separating the magnetic signal of the EEJ from that of the solar quiet conditions currents and from the magnetospheric ring currents as shown for the first time by *Rastogi & Klobuchar* [1990] [see also *Manoj et al.*, 2006].

We computed ΔH at both observatories by subtracting to the time series of the H component its long term trend and continuous component: we evaluated, for each day with daily average Kp<1 from 08 August 2018 to 09 September 2018, $H_{1:4}$ LT, i.e. the average over the time interval 01-04 LT (which is statistically the geomagnetic quietest time interval in a day); then we fitted the $H_{1:4}$ LT time series with a linear fit. Then, ΔH is retrieved as $\Delta H = H - (A \cdot t + B)$, where t represents the time and A and B are the coefficients derived by the least mean square regression analysis. We remark that the linear fits at the two stations are practically coincident. Furthermore, in order to identify the EEJ variations, we compute the difference $\Delta(\Delta H) = \text{EEJ} = \Delta H_{TTB} - \Delta H_{KOU}$.

For depicting the behavior of EEJ for regular variations, hereafter $\Delta(\Delta H)_R$, a Superimposed Epoch Analysis (SEA) has been performed by using the same data of KOU and TTB used to define $<H_{1:4\ LT}>$.

To remove geomagnetic fluctuations at short periodicities in the components, the magnetic data are smoothed by performing a moving average over about 1-hour time window, with a step size of 1 minute.

Since $\Delta(\Delta H)$ shows an almost Gaussian distribution, both composite $\Delta(\Delta H)_C$ and its related standard error of the mean (SEM_C) are computed in order to establish the confidence interval at 1% confidence level as $\Delta(\Delta H)_R = \Delta(\Delta H)_C \pm 2.58\ SEM_C$ [*Laken and Čalogović*, 2013; *Regi et al.*, 2017].

2.3. **Ground-based Ionospheric data**

2.3.1. **GNSS data**

We leverage on the ground GNSS receivers (blue dots in Figure 1) included in the Rede Brasileira de Monitoramento Contínuo (RBMC) network managed by the Instituto Brasileiro de Geografia e Estatística (IBGE). Such receivers provide data in RINEX format with a time resolution of 30 seconds. By applying the calibration technique introduced by *Ciraolo et al.* [2007], we derive the slant Total Electron Content (sTEC) for each couple receiver-satellite. Then, we estimate the vertical Total Electron Content (hereafter vTEC) by applying a thin-shell approximation, by assuming an Ionospheric Piercing Point (IPP) located at 350 km [see, e.g. *Mannucci et al.*, 1998] and by considering an elevation angle mask of 20°. Values of vTEC covering the field of view of the receivers are interpolated by using natural neighbors' method to derive vTEC maps [*Cesaroni et al.*, 2015].

To compare the N_e measured at LEO altitudes with the TEC information, vTEC has been evaluated along each considered Swarm A and CSES-01 tracks. The along-the-track-vTEC ($vTEC_{att}^{Sat}$) has been retrieved by considering the corresponding vTEC maps. Such maps have been calculated by interpolating vTEC measurements covering an interval corresponding to time range in which the given satellite passes in the latitudinal range between 10°N and 35°S, being the time interval reported in Table 1.

Thus, by definition:

$$vTEC_{att}^{Sat}(\varphi, \lambda) = vTEC(\varphi = \varphi^{Sat}, \lambda = \lambda^{Sat}), \tag{1}$$

where φ^{Sat} and λ^{Sat} are the longitude and latitude of the track of the LEO satellites, respectively, and $Sat = (SwarmA, CSES - 01)$.

To check for the possible presence of scintillation on GNSS signals [*Kintner et al.*, 2009], that may reveal the presence of small-scale (below few hundreds of meters) irregularities embedded in EPBs, we also checked the scintillation data provided by the CIGALA (Concept for Ionospheric Scintillation Mitigation for Professional GNSS in Latin America)/CALIBRA (Countering GNSS high Accuracy applications Limitations due to Ionospheric disturbances in BRAzil) network [*Vani et al.*, 2017]. No scintillation events were recorded and then such data are not included in the analysis.

In addition, 5-minutes rate of TEC index (ROTI) values [*Pi et al.*, 1997] calculated from the RBMC data have also been investigated. ROTI is able to detect the presence of ionospheric irregularities having typical scale size up to few kilometers [see, e.g., *Alfonsi et al.*, 2011 and references therein], as those characterizing the EPBs. Again, although small ROTI enhancements have been found during nighttime on 26 and 29 August for some radio links in the western Brazilian sector (not shown), they are almost below the 0.5 TECu per minute threshold, suggested by *Alfonsi et al.* [2011] to identify ionospheric irregularities at scale lengths of a few kilometers and above.

2.3.2. **Ionosonde data**

Ionosonde data have been analyzed to investigate the ionospheric behavior at the F-layer altitudes. Ionospheric parameters have been manually scaled from hourly-recorded ionograms through the *Interpre* software [*Pezzopane*, 2004] at the ionospheric stations of São Luís (2.6ºS; 44.2ºW) and Cachoeira Paulista (23.2ºS; 45.8ºW) (red squares in Figure 1). Between the two, São Luís is the closest to the magnetic equator, while Cachoeira Paulista usually behaves as a crest station under solar maximum conditions, even if under low EEJ intensity conditions (typical of low solar flux and winter conditions) may behave like a mid-latitude station [see., e.g., *Muella et al.*, 2017]. According to our knowledge, data from such ionosondes were the only available during the storm in Brazil.

Time series of the F2-layer critical frequency (f_oF2) and the estimate of the peak altitude (h_mF2) from 24 to 31 August 2018 are here considered and compared with quiet time behavior, defined by the $\pm1\sigma$ band around the mean value in the selected quiet reference period (days with daily Kp<1 in the range 08 August 2018 to 09 September 2018). The value of f_oF2 is proportional to the ionospheric ionization peak value (N_mF2) through the relation:

$$N_mF2 = 1.24 \times 10^4 (f_oF2)^2, \tag{2}$$

where N_mF2 is expressed in cm^{-3} and f_oF2 in MHz. Values of f_oF2 are directly scaled from ionograms, while h_mF2 is estimated by the widely used *Shimazaki* [1955] formulation:

$$h_mF2 = \frac{1490}{M(3000)F2} - 176, \tag{3}$$

which assumes an F2-layer with no underlying ionization, and neglects the geomagnetic field [*Elias et al.*, 2017]. Indeed, the values of the M(3000)F2 factor are traditionally used to estimate

h_mF2 by means of equation (3) or more sophisticated expressions that require the use and the scaling of other characteristics [e.g. *Dudeney*, 1983; *McNamara*, 2008]. Hence, values of h_mF2 are not the physical F2-layer maximum heights but an empirical approximation [see, e.g., *Perrone et al.*, 2018]. To constrain the h_mF2 values to the actual observations, manually scaled values of the M(3000)F2 factor have been used in equation (3). In particular, M(3000)F2 is automatically calculated by the *Interpre* software dividing the MUF(3000)F2 value by f_oF2, where MUF(3000)F2 is scaled from the ionograms through the transmission curve method [*Pezzopane*, 2004]. The standard uncertainty in scaled values of f_oF2 is ±0.1 MHz, while for M(3000)F2 it is ±0.05 [*Piggot & Rawer*, 1972] plus a random component raising it to 0.1, which would correspond to a h_mF2 uncertainty of about 15 km using the Shimazaki formula [*McNamara*, 2008; *Elias et al.*, 2017]. However, the h_mF2 results obtained at Cachoeira Paulista by using the Shimazaki formulation were not consistent. To overcome this issue, autoscaled h_mF2 obtained by *Autoscala* software [*Scotto & Pezzopane*, 2002; *Scotto*, 2009] have been used, after being manually checked in order to exclude unreasonable values. Although this operation reduces the amount of data, this reduces the statistical inaccuracy (from about 16.6 km up to 34.1 km, depending on the conditions) associated with Autoscala h_mF2 estimations, particularly under harsh geomagnetic conditions [*Scotto & Sabbagh*, 2020].

In addition, vTEC over the ionosonde is estimated similarly to $vTEC_{att}^{Sat}$, i.e. by exploiting equation (1) evaluated at the ionosonde locations ($\varphi = \varphi^{ionosonde}, \lambda = \lambda^{ionosonde}$) and by considering vTEC maps covering 10 minutes intervals.

To identify the quiet behavior for the ionospheric parameters, the same period used for the ground-based magnetic data has been considered and the quiet reference is provided in terms of the ±1σ variation around the mean.

2.4. **Geospace conditions and activity indices**

The analysis of the geospace conditions during the storm is based upon the measurements of the Interplanetary Magnetic Field (IMF) and solar wind (SW) parameters as measured by satellites missions in the upstream region, provided by OMNI database and available on CDAWeb (https://cdaweb.gsfc.nasa.gov/index.html/). Specifically, we take into account the IMF total intensity (B) and its north-south component (B_z), radial component of the SW velocity (V_x) and

SW pressure (P_{sw}). In addition, the zonal component of the Interplanetary Electric Field (IEF) is computed from the product $V_x \cdot B_z$ [see, e.g., *King & Papitashvili*, 2005; *Weimer et al.*, 2017]. The relative behavior of P_{sw}, B, B_z and IEF is the key-factor to understand the solar wind-magnetosphere-ionosphere-thermosphere (SW-M-I-T) coupling processes and, in particular, the manifestation of PPEFs and DDEFs, generated at high-latitude and influencing also the low-latitude ionosphere [*Manoj et al.*, 2006, 2008, 2013; *Fejer*, 1991, 2011; *Fejer et al.*, 2005, 2017]. Indeed, an estimate of the variation of the EEF driven by PPEF can be provided by a proper transfer-function obtained from coherence analysis between IEF and EEF, as in *Manoj et al.* [2008, 2013] and *Manoj & Maus* [2012].

All parameters have a 5-minutes time resolution, according to *Manoj et al.* [2008], and are time shifted to Earth's bow shock, to provide a picture as close as possible to the one reaching the magnetosphere. This also enables an immediate comparison between magnetospheric and ground observations. For a practical purpose, the disturbance to the EEF (*ΔEEF*) can be estimated by using the most convenient digital filter that operates directly in the time domain on the IEF time series [see e.g., *Smith*, 2007]. Then, to consider the effect at the Brazilian longitude, the time series is corrected for the local time scaling derived by *Manoj & Maus* [2012] from correlation analysis between IEF and EEF: a positive IEF produces to a positive/negative disturbance to EEF at noon/midnight.

The method to derive *ΔEEF* is then a 2-steps process:

Step 1.   the EEF variations at noon were obtained applying the digital filter on IEF data at 5-minute time resolution time-shifted to the bow shock nose provided by OMNIWeb, and then adding the delay time for the propagation of disturbances from bow shock to ground; the latter quantity, estimated through the best correlation between geomagnetic and interplanetary data, is equal to 15 minutes value (3 samples) accordingly with ~17 minutes empirically derived [e.g. *Manoj et al.*, 2008];

Step 2.   through a time scaling factor, *ΔEEF* at noon is converted to *ΔEEF* at local time of the geomagnetic station [*Manoj & Maus,* 2012].

To provide a measure of the geomagnetic activity at low latitude mainly due to ring-current intensity variations, the SYMH index (5-minutes resolution) is also taken into account [see, e.g., *Li et al.*, 2011]. To speculate about the role of DDEFs in the found ionospheric variations, as they

are mainly driven by changes in the neutral wind circulation possibly triggered by ionospheric heating at high-latitude, the local Joule heating j, due to the dissipation effects of FAC and auroral electrojet, is considered as well. The value of j is a function of the latitude and longitude and it is estimated by using the high-latitude ionospheric electrodynamic model developed by *Weimer* [2005a, 2005b]. The value of j is computed on a grid with a spatial resolution of $1°\times1°$ over the polar cap region, ranging from 60° to 90° S and N.

We evaluate the polar cap Joule heating by defining J_h as the average of j over the entire polar cap, for each hemisphere: the time resolution of J_h is 1 hour.

3. **Results**

Figure 2 shows the time evolution from 24 to 31 August of the IMF B and B_z, of SW V_x and P_{sw}, of the IEF, of the *ΔEEF*, adjusted for intermediate geographic local time between the two geomagnetic observatories, i.e. using the local time scaling function according to *Manoj et al.* [2008], of the SYMH index and J_h for the northern (blue) and southern (red) polar caps. The yellow vertical areas indicate the range between 16:00 UT and 18:00 UT, to highlight the times of the passages of the LEO satellites over the considered region.

The pre-storm conditions during 24 August are characterized by a small and broad peak of P_{sw} between 06:00 UT and 14:00 UT (up to 4 nPa at 12:10 UT), in correspondence of which fluctuations of the IEF and B_z, swinging among positive and negative values are found. At 12:10 UT, i.e. at the time of the peak P_{sw}, the southward turning of the B_z results into: (i) a PPEF event able to increase eastward the EEF of about 0.13 mV/m; (ii) raising of heating in the polar caps, whose peak is reached at 14:00 UT (J_h up to 4.6 mW/m^2 for the northern polar cap, 2.1 mW/m^2 for the southern).

As already noticed by *Astafyeva et al.* [2020], the CME structure arrived to the Earth at 02:45 UT on 25 August without providing the classical signature of a Sudden Storm Commencement on the SYMH [see also *Piersanti et al.*, 2020, for details], that during the day reveals rather the signature of the magnetospheric compression due to the increased P_{sw}. This effect can also be seen in the correspondence among the three P_{sw} peaks (at about 08:30, 11:00 and 13:20 UT) during 25 August and the peaks of SYMH right before the main phase of the storm. At about 16:10 UT (~13:10 LT in Brazil) on 25 August, the open lines configuration of the magnetosphere following the southward flipping of B_z, resulted into a small but impulsive eastward intensification of the

14

EEF, indicating a dayside PPEF event, and a significant increase of the particle precipitation along the magnetic field lines and current dissipation, resulting into a corresponding increase of J_h. As per the time evolution of J_h, the effect of the storm on the particle precipitation favors the northern hemisphere, both for the starting time of activity and for its intensity. This may result in interhemispheric differences in the ionospheric behavior at low-latitude, due to both different meridional winds modifying the EEJ through DDEFs and different composition effects changing the background plasma density. The peak of the storm is reached on 26 August at ~07:00 UT, under long lasting southward conditions of the IMF. The beginning of the following recovery phase is featured by oscillations of IEF/B_z under strong B conditions (up to about 18 nT) until ~22:30 UT. These also trigger the oscillations found in J_h, with a similar impact on both hemispheres. During this period, the SYMH time profile shows substorm-like signatures, that have been hypothesized to be driven by the effect of a Corotating Interaction Region (CIR) [*Piersanti et* al., 2020], and the most significant variations of the EEF linked to the PPEF take place. The recovery phase of the storm is featured by SW speed higher than about 400 km/s and oscillations of IEF/B_z that correspond to meaningful oscillations in the heating activity, quite symmetrically on the polar caps of both hemispheres: indeed, CIR-driven geomagnetic storms are able to induce relativistic particle acceleration, enhanced magnetospheric convection and ionospheric heating [*Pokhotelev et al.*, 2009].

Figure 3a shows the variations of the horizontal H component of the magnetic field *ΔH* at TTB (red) and KOU (black) observatories. The behavior of both time series clearly shows the occurrence of the geomagnetic storm, with a decrease starting on late 25 August that follows the arrival of the impinging interplanetary structure. The storm peaks early on 26 August (approximately -120 nT) and the consequent recovery phase lasts several days. The response to the geomagnetic storm at both stations is very similar, as expected since the latitudinal separation is smaller than the spatial length scale of the ring current effects. Figure 3b reports the outline of EEJ = *ΔH*$_{TTB}$ - *ΔH*$_{KOU}$ (black line), of the reference difference for quiet conditions *Δ(ΔH)$_R$* (green strip), of the *ΔEEF* (red line, same as in Figure 2) and of the EEF derived by Swarm A measurements (black dots). Similarly to Figure 2, the yellow vertical areas indicate the time range between 16:00 UT and 18:00 UT, matching the times of the LEO satellites passages over the Brazilian region. *Δ(ΔH)$_R$* shows the statistically expected behavior of the EEJ at Brazilian longitudes [see, e.g., *Rastogi*, 2007]. In the specific: (i) a negative peak (westward current) at about

10:30 UT (07:30 LT), which identifies the morning CEJ (MCEJ); (ii) another negative, less intense, peak at about 18:00 UT (15:00 LT), being the afternoon CEJ (ACEJ) and a positive peak (eastward current) at about 14:00 UT (11:00 LT) corresponding to the strong midday EEJ. These features are well in agreement with the recent findings by *Soares et al.* [2018], who showed that $\varDelta(\varDelta H)$ at TTB and KOU observatories exhibits two CEJs in the morning and afternoon hours, differently from a couple of Peruvian observatories at a similar latitude. The authors propose that the observed difference could be due to the presence of the SAMA. Moreover, *Soares et al.* [2018] observed that both morning and afternoon CEJ occurrence rates attain maximum levels during June-August months, which well explains our observations (see in particular the $\varDelta(\varDelta H)_R$).

In order to investigate the different factors contributing to the EEJ variations, we may consider that EEJ strength, given by $\varDelta(\varDelta H) = \varDelta H_{TTB} - \varDelta H_{KOU}$, is the sum of three main contributions:

$$EEJ \simeq \varDelta(\varDelta H)_R + \varDelta(\varDelta H)_{PPEF} + \varDelta(\varDelta H)_{DDEF} \tag{4}$$

in which $\varDelta(\varDelta H)_{PPEF}$ and $\varDelta(\varDelta H)_{DDEF}$ refer to the variations induced by PPEF and DDEF, respectively. We also remark that the equation (4) represents a good approximation of the observed geomagnetic variations, since neither SEP events nor geomagnetic SF are present during the examined time interval. The sign of $\varDelta(\varDelta H)_{PPEF}$ depends on daytime/nighttime conditions and on the flipping of the IMF B_z [*Wei et al.*, 2015]. For instance, during daytime $\varDelta(\varDelta H)_{PPEF}$ is positive (negative) if B_z flips southward (northward), while during nighttime the sign is the opposite. Conversely, the sign of $\varDelta(\varDelta H)_{DDEF}$ is directed westward during daytime and eastward during nighttime, i.e. always acting as anti-solar quiet behavior [*Yamazaki & Maute*, 2017]. However, as per its definition, the sign of EEF must be the same of $\varDelta(\varDelta H)_{PPEF}$, because $\varDelta EEF$ is the best estimate of the variation to the Equatorial Electric Field driven by the sole PPEF (see Section 2.4). The sign and entity of $\varDelta(\varDelta H)_{DDEF} + \varDelta(\varDelta H)_{PPEF}$ can be derived by comparing the black curve with green stripe reported in Figure 3b. Finally, the $\varDelta EEF$ time variations (red curve) are used to provide an indirect estimation of the intensity of $\varDelta(\varDelta H)_{PPEF}$.

It is worth noticing the general disagreement between EEF from Swarm A and EEJ during the early stage of the storm (25-27 August), while the two agree in the late recovery phase (from 28 onwards). This is likely due to possible biases in the subtracted magnetospheric field models when processing Swarm scalar field measurements do derive EEF measurements under the most disturbed conditions triggered by the geomagnetic storm.

During 24 August, small negative deviations from $\Delta(\Delta H)_R$ are found in correspondence with the MCEJ and ACEJ. It is noteworthy that at 12:10 UT the ΔEEF increases of about 0.12 mV/m following the PPEF event, probably due to the P_{sw} peak and corresponding southward flipping of the IMF B_z, is not able to increase the EEJ, as $\Delta(\Delta H)$ is well inside the quiet time variations. This may be due to the fact disturbance-dynamo effects are already in place, balancing the daytime eastward additional electric field due to the PPEF event with a westward component.

During 25 August, no significant deviation from the quiet behavior is recorded until 12:25 UT. Right after, CEJ conditions remain almost until the end of the day. These CEJ conditions are not found in the West South American (Peru) sector, as Figure 2c of Astafyeva et al. [2020] reports, in which only a depletion of the EEJ is found by using Jicamarca (76.8°W; 11.9°S) and Piura (80.6°W; 5.2°S) magnetic observations. This intriguing feature found during the main phase of the storm is in correspondence with the decrease (at 14:20 UT) and then increase of the EEF (ΔEEF up to 0.14 mV/m at 16:40 UT) found in correspondence with the peak conditions of the storm-driven daytime CEJ. In this case, CEJ conditions are also confirmed by the sign of the EEF measured by Swarm.

As already reported in Figure 2, the behavior ΔEEF is clearly justified by the effect of PPEF, due to the flipping of the IMF B_z (and hence of the IEF) under increased value of the total field B. However, if PPEFs were the only actor, an increase of the daytime EEJ would have taken place, but this is not the case. This indicates that the signature of EEJ during daytime on 25 August is ruled out by DDEFs, driven by the sudden and meaningful increase of the heating at auroral latitudes of both hemispheres. The heating starts raising at 12:00 UT (Figure 2h), i.e. about 2.5 hours before the beginning of the B_z/IEF turning and it is due to the magnetopause compression, as suggested by the P_{sw} peaks between 08:30 and 13:20 UT (Figure 2d). The identified timing is in agreement with the expected one for DDEFs effect.

The most disruptive effects to ionospheric electrodynamics are found on 26 August, when new and strong CEJ conditions are found. CEJ conditions are also found in the Western South American sector, as Figure 2c of Astafyeva et al. [2020] reports. In such a sector, EEJ conditions are restored at about 20 UT, while in the Brazilian sector last almost for the whole day. These are driven by the interplay of strongest PPEF and DDEF events of the storms, identified by the oscillation of the B_z/IEF (Figure 2b/e) and by the J_h increase (Figure 2h), respectively. In the

specific, eastward *ΔEEF* values are found (peaks at 15:25 UT and 19:25 UT) and westward (13:25 UT and 18:05) alternates. While the expected PPEF event peaking at 15:25 UT is able to lower the CEJ intensity, the overall westward disturbance due to the summing up of the DDEFs and PPEFs events at 13:25 UT and 18:05 UT is maintained for the rest of the day.

During 27 August, the morning CEJ is present but with a smaller intensity with respect to regular conditions, while daytime EEJ and afternoon CEJ are significantly larger. During the later stages of the recovery phase, when perturbations in EEF and in J_h are less intense, due to the recovery from unsettled conditions, increased values of the daytime EEJ are found on 28, 29 and 31 August, confirmed also by the behavior of the EEF Swarm. The pattern is an amplitude modulation of EEJ/CEJ peaks of $\Delta(\Delta H)_R$, having a period roughly estimated to be in the range between 2 to 5 days as derived through wavelet analysis (not shown), being compatible with planetary waves, or Rossby waves, as reported in section 4.3.2 of *Yamazaki & Maute* [2017].

From Figure 3b also the behavior of 31 August is intriguing, as the EEJ is not only enhanced (up to about 62 nT), but also presents a double peak: a first one in correspondence with the maximum of $\Delta(\Delta H)_R$ (and of the same intensity), while the second one is at about 16:50 UT, i.e. at later times and well in correspondence with Swarm-A and CSES-01 passages. This may be due to the joint effect of a small PPEF event and to the increased magnetospheric compression, following the P_{sw} broad peak (Figure 2d) in the day and occurring under IMF total field conditions of about 8 nT (Figure 2a).

Also the possible effects due to variations in conductivity and/or electric field of the ionospheric regions above the observatories, due to particle precipitation from the inner radiation belt, have been tested as a hypothesis for the EEJ intensity in the recovery phase. This has been investigated through the Total Energy Detector (TED) electron/proton energy fluxes at 120 km, derived from all available Polar Orbiting Environmental Satellites (POES) data (https://www.ngdc.noaa.gov/stp/satellite/poes/dataaccess.html), collected at an average altitude of ~840 km, by comparing TED levels of quite days with that collected during 28-30 August 2018. The results (not shown here) suggest that particle fluxes do not contribute significantly to ionospheric conductivity changes.

The aim of Figure 4 is to depict the possible signatures of the formation of EIA crests at LEO altitudes during the different phases of the storm and the relative behavior of N_e and vTEC. Left

18

plot in each panel of Figure 5 shows the value of N_e as measured by Swarm A (blue) and CSES-01 (red) satellites. Differently from what reported in Table 1, such plots consider a latitudinal range of the selected tracks that covers up to 35°N, to investigate the latitudinal sector in which the northern crest of the EIA may manifest. The relative maxima are indicated with a dashed line, according to the same color code. Time intervals refer to quiet geomagnetic conditions (10 August, panels a and b), pre-storm (24 August, panel c and d) and storm conditions (25 to 31 August, panels from e to r). Top right text in each map of Figure 4 reports the time intervals of the selected tracks, as also indicated in Table 1. As per such a table, the vTEC maps integrate measurements covering 11 or 12 minutes, depending on the day. In each vTEC map (right plot of each panel), ground tracks of Swarm A (thin blue line) and CSES-01 (thin red lines) are reported, while the blue and red thick lines indicate the *in situ* electron density by Swarm A and CSES-01, respectively. The larger the longitudinal positive deviation from the ground track, the larger the corresponding electron density. We let the reader notice that scales on both y-axes are not fixed, to enable the day-by-day comparison of the latitudinal behavior of TEC_{att} and N_e from Swarm A and CSES-01.

To complete the picture of the EIA crests during the storm provided through Figure 4, the distance (in degrees) of the electron density maximum/maxima for Swarm A and CSES-01 from the magnetic equator are reported in the top and bottom panels of Figure 5, respectively. The distance of the electron density maximum/maxima from the magnetic equator is estimated by calculating d_{ME}, according to the following relation:

$$d_{ME} = \lambda(Max(Ne)) - \lambda_{ME}^{Sat}, \tag{5}$$

where $\lambda(Max(N_e))$ is the latitude in degrees North of the N_e relative maxima or absolute maximum and λ_{ME}^{Sat} is the latitude of the magnetic equator crossed by the satellite orbit.

N_e values measured by Swarm A are larger than those by CSES-01, being the ratio of the maxima in N_e scale ranging from about 5 to about 7.5 times. This is in agreement with what reported in Section 2.1 about the issue concerning the N_e ratio between Swarm A and CSES and with the low ratio regime, whose compensation factors are already described.

The quiet conditions on 10 August results in a single peak of electron density located almost in correspondence with the magnetic equator, as shown by the distance between the vertical red/blue and orange dashed lines in the left plots of Figure 4a-b. For what concerns the corresponding vTEC behavior, both $vTEC_{att}^{SwarmA}$ and $vTEC_{att}^{CSES-01}$ present a single peak that fits with the magnetic equator

19

for Swarm A, while it is southward displaced for CSES-01. Such displacement is likely due to the coverage of the vTEC mapping that does not allow to properly cover the magnetic equator sector. This single peaking is found for both integrated and *in situ* N_e measurements. This agrees with the climatological behavior of the vertical plasma drift, that is found to be minimum in the southern hemisphere winter months and under low solar flux [see, e.g., *Fejer*, 1991].

The pre-storm conditions on 24 August result into a single broad N_e peak for Swarm A, whose maximum is located at 9°N (d_{ME}=11°), while two broad peaks can be identified for CSES-01: one at about 17°N and one at about 19°S, resulting to be quite symmetrical with respect to magnetic equator but more pronounced in the northern hemisphere. On the same day and for both time intervals, vTEC$_{att}$ seems to present a single peak located roughly in correspondence with the position of the magnetic equator, which is in agreement with the behavior under quiet conditions. However, the map coverage limits the possibility to identify if actually TEC behaves differently from *in situ* N_e. The deviation of the pre-storm conditions to quiet behavior is an intriguing feature of the storm that may be related to transport phenomena driven by the auroral activity on 24 August, as reported by the time profile of J_h (Figure 2), that also indicate the different global thermospheric circulation in the two hemispheres, which can be identified as a possible responsible for the found interhemispheric asymmetry.

During 25 August, vTEC from maps is slightly depleted with respect to the pre-storm conditions. On this day, Swarm A and CSES-01 pass right before the SYMH drop (Figure 2g) and in correspondence with the second minimum of EEJ in the day (Figure 3b). The depleted ionization is the effect of the CEJ (Figure 3b), that inhibits the **ExB** plasma uplift. This results into a similar pattern of N_e and vTEC$_{att}$ with respect to the pre-storm conditions, but with depleted values, because of the CEJ conditions. The N_e maxima at LEO altitudes are similar to 24 August, revealing that also on the 24 a small and broad peak of N_e may be present in the southern hemisphere even at Swarm A altitudes. The maxima are quite symmetrical with respect to the magnetic equator. The different distance between N_e peaks for Swarm A and CSES-01 follows from different magnetic field intensity at different altitudes, as expected at equatorial regions. The values of N_e are larger for the northern hemisphere, likely due to different transport phenomena changing the thermospheric composition in a different way in the two hemispheres during storm commencements [see., e.g., *Abdu*, 1997]. This is also confirmed by the already mentioned different behavior of J_h (Figure 2h), increasing sooner and being larger in the northern hemisphere, and by

what reported in the neighboring Peruvian sector at 77°W by *Astafyeva et al.* [2020], reporting the changes in composition recorded by the GUVI/TIMED satellite. Similarly to 24 August, the corresponding values $vTEC_{att}^{SwarmA}$ and $vTEC_{att}^{CSES-01}$ (Figures 4e-f) seem to present a single peak that tends to be located in correspondence with the magnetic equator. We report some limitations in evaluating the $vTEC_{att}^{Sat}$ behavior due to the fact that the satellite crosses the magnetic equator and the map boundary, bringing then some small border effects in evaluating the TEC along-the-track.

On 26 August, the LEO satellites passed in correspondence with the early recovery phase of the storm, which is characterized by geomagnetic variations in correspondence with oscillating B_z, IEF and ΔEEF (Figure 2, panels b, e and f), resulting in strong CEJ conditions (Figure 3). The latitudinal profile of the *in situ* electron density results into a single peak for both Swarm A and CSES-01, as per depleted **ExB** under strong CEJ conditions.

In the case of CSES-01, the peak perfectly matches the magnetic equator, while for Swarm A, a small displacement is found. This is likely due to the fact that the Swarm A pass covers the vTEC peak at mid-latitude, possibly resulting in the poleward displacement of N_e peak for Swarm, while at the CSES-01 passage, the mid-latitude increase has significantly lowered down. This is visible in the vTEC maps, which show the combined effect of the high variable EEJ and of a positive ionospheric storm at mid- and low-latitudes.

In the specific, in the equatorial region the vTEC pattern seems to follow the CEJ conditions, with a single peak at the magnetic equator, clearly depicted in correspondence of the CSES-01 pass (Figure 4h) and less visible on Swarm A data (Figure 4g), because the latter is featured by the increased vTEC at mid-latitudes, as will be better described through ionosonde data. The features found at LEO altitudes are confirmed by the latitudinal behavior $vTEC_{att}^{Sat}$, as $vTEC_{att}^{CSES-01}$ presents a peaked structure in correspondence with the magnetic equator, while the poor spatial coverage from which $vTEC_{att}^{SwarmA}$ is derived allows reporting the mid-latitude enhancement but it does not provide information at the magnetic equator. It is worth noticing that, as per both Figures 4 and 5, the N_e increase with respect to the 25 August is evident for Swarm A (being almost doubled), while it is of the same order of magnitude for CSES-01. This may be due to the fact the CSES-01 covers higher altitudes of the topside ionosphere with respect to Swarm A, resulting in a weaker variability.

In other words, when CEJ conditions stands instead of EEJ, the absence of an **ExB** uplift induces the low-latitude ionosphere to behave similarly to at mid-latitudes, showing negative storm effects in northern and positive storm effects in the southern, whose asymmetry is driven by different global thermospheric circulation due to seasonality.

On 27 August, the storm is in its recovery phase (as per SYMH in Figure 2). The LEO satellites tracks are in correspondence with enhanced EEJ, oscillating EEF and enhanced Joule heating in the polar cap. At the local magnetic response, the EEJ is enhanced on 27 August (EEJ~40 nT). Even if the LEO satellites pass over Brazil right after it, the vTEC maps indicate clear crest signatures peaking between 5° and 10°. The latitudinal profile of the *in situ* electron density for Swarm A and CSES-01 depicts the double peaked structure also at LEO altitudes. This is particularly evident for Swarm A, whose N_e profile is almost symmetric (as also reported on Figure 5) and with the trough located exactly in correspondence with the magnetic equator. The N_e is larger in the northern hemisphere with respect to the southern one. CSES-01 presents some scattered data that may pose some limitations in the reconstruction of the peak in the northern hemisphere. However, the less evident crest signature at CSES altitudes may be related with the different altitudes of the two satellites, as they probe different intensity of the **ExB** drift. The latitudinal profile of both $vTEC_{att}^{Sat}$ confirms the crest signatures found with *in situ* plasma density data. It is interesting to note that $vTEC_{att}^{Sat}$ peaks are at poleward latitudes with respect to N_e peaks. This is justified by the altitude-latitude variations of electron density [see, e.g., Figure 2 of *Balan et al.*, 2018], as the bulk of $vTEC_{att}^{Sat}$ comes from the F-layer peak, poleward displaced with respect to N_e peak at LEO altitudes.

The EIA crest signatures are found again in vTEC, N_e from LEO satellites and $vTEC_{att}^{Sat}$ on 28, 29 and 31 August, when the EEJ conditions differ from the regular behavior mostly for the EEJ day-to-day variability, mainly due to the irregular variability in the neutral wind, and by the presence of the aforementioned planetary waves. At LEO altitudes, the crests are better depicted by Swarm A satellite than by CSES-01, because of the different orbital heights (460 and 507 km, respectively). In fact, on the average the crests of the equatorial anomaly forms at height below 500 km, while above only a maximum above the geomagnetic equator is formed [Rishbeth & Garriot, 1969].

As already specified when discussing Figure 3, the EEJ peak on 31 August is delayed to 16:50 UT (i.e. at the time of the LEO passes), likely because of a further magnetosphere compression, resulting in the clearer crest signature at CSES altitudes of the whole period.

Except at CSES-01 altitudes on 27 August, when the crests are present, they appear geographically symmetric around the magnetic equator, where the density trough is located, and are asymmetric in N_e values favoring the northern hemisphere (Figure 5). Such interhemispheric asymmetry of N_e values follows from the interplay of seasonality, favoring the northern hemisphere, and Joule heating, that is, on average, larger in the northern hemisphere (Figure 2). The crest signature is lost on 30 August (see also Figure 4, panels o and p), when EEJ is similar to the regular behavior (Figure 3). The relative behavior between N_e and $vTEC_{att}^{Sat}$ is also confirmed in these days of storm recovery.

To further confirm the differences in the ionospheric response to the storm at equatorial and mid-latitudes, Figures 6 and 7 show time series of the hourly values h_mF2 (panel a), f_oF2 (panel b) and vTEC (panel c) over the ionosonde compared to the quiet reference at the ionospheric stations of Cachoeira Paulista and São Luís, respectively. In the figures, yellow-shaded boxes highlight the daytime passes of Swarm A and CSES-01, ranging between 16:00 UT and 18:00 UT (see intervals in Table 1).

The measurements over Cachoeira Paulista (Figure 6) present a significant positive variation with respect to the quiet behavior from 26 to 29 August and on 31 August, in the diurnal hours (10:00 UT -21:00 UT), and in particular in the hours corresponding to the LEO passes. The concurrent f_oF2, vTEC and h_mF2 increases observed on 26 August, under storm-induced daytime CEJ conditions, shows that Cachoeira Paulista is exposed to a mid-latitude ionosphere mechanism, triggered by equatorward thermospheric wind and probably due to an increase of [O] which is observed in height-integrated [O]/[N$_2$] ratios from GUVI/TIMED satellite (see Figure 5, row A, of *Astafyeva et al.* [2020]). This is also confirmed by the average neutral density measured by Swarm C (not shown), that, on the average, peaks up to about $9.5 \cdot 10^{-13}$ kg/m^3 on 26 August (reference quiet value is in the range $2 \div 3 \cdot 10^{-13}$ kg/m^3) and recover to quiet conditions roughly from 29 August. The positive storm signatures on 26 August are also recorded at the equatorial São Luís station (Figure 7) and at a neighboring mid-latitude station of Bahia Blanca (Argentina, 38.7ºS; 62.3ºW). From 28 August onward, the positive deviations are likely due the fact that the

formation of the southern crest of the EIA contributes to the rise of the ionization over Cachoeira Paulista.

For what concerns São Luís (Figure 7), which depicts the behavior close to the dip equator (Figure 1), the CEJ conditions on 25 August lower the value of h_mF2, while f_oF2 values remain near to the quiet reference, as expected under CEJ conditions. In correspondence, vTEC values are also slightly depleted. As already noted, on 26 August, positive storm effects are observed in f_oF2 and vTEC, with h_mF2 comparable with the lower boundary of the quiet reference during daytime, due to the decrease of the normal eastward electric field conditions. On 27 August, the larger deviation from vTEC quiet behavior was found, with a slight increase in f_oF2 during LEO satellites passages, and h_mF2 next to the upper boundary of the quiet reference level. From 28 August f_oF2 and h_mF2 are near to the background value due to the restoring of the EEJ conditions.

The main controlling parameter of the day-to-day equatorial N_mF2 variations is vertical **ExB** plasma drift, which in this case is upward. The irregular variability in the neutral wind is considered to be the main source of the EEJ daily variability [*Yamazaki & Maute*, 2017].

4. **Summary and conclusions**

Leveraging on the multi-sensor approach here adopted, we highlight the ionospheric variations in the topside and bottomside ionosphere occurring during the different phases of the August 2018 storm. As already reported in the work by *Astafyeva et al.* [2020], the storm presents several peculiarities: being under slowing down conditions of the solar winds, its gradual beginning, the difficulties in being forecasted and the interhemispheric differences in terms of ionospheric response. We cover the Brazilian longitudinal sector and we investigate the ionospheric response from the pre-storm to the late recovery phase conditions of the storm, focusing on the time interval between 16:00 UT and 18:00 UT. Such interval is featured both by the closeness to the time of the expected maximum of the EIA intensity, and by the daytime passes of both Swam A and CSES-01 satellites. The seasonal and solar cycle conditions are such that the **ExB** is at its minimum. Through the considered instruments we are able to provide a detailed picture from low- to mid-latitudes over the area of interest. With the proposed approach, we are also able to highlight the relative role of PPEF and DDEF in the resulting EEJ variability in the main and early recovery phases of the geomagnetic storm (25-27 August). We aim at completing and extending the picture

provided by *Astafyeva et al.* [2020], which investigated the storm development in the Western South American (Peru) sector at 77°W during 25 and 26 August 2018. Significant longitudinal difference between the Western and Eastern South American sectors is found, because of the different local time of the storm development and the presence of the SAMA, resulting mainly into CEJ conditions during daytime of both 25 and 26 August in the Brazilian sector. This is different with respect to what was found by Astafyeva et al. [2020] in the Peruvian sector, where only EEJ depletion is found on 25 August, while both EEJ and CEJ conditions follow each other on 26 August.

In the pre-storm conditions, negative deviations from the regular behavior is observed related to the Joule heating, and to fluctuations of the IEF/B_z, inducing PPEF, which also contributes to the observed interhemispheric differences and reinforcing the North-South asymmetry in the thermosphere due to transequatorial winds from South to North is present under quiet conditions, favoring the plasma transfer to the northern crest [*Barlier et al.*,1974].

On 25 August a whole-day CEJ is recorded, and we retain that it is due to variations triggered by DDEFs that are stronger than those by PPEFs. Such control could probably be driven by the sudden and meaningful increase of the heating at auroral latitudes of both hemispheres and by magnetospheric compression.

The weak ionospheric response at the beginning of the storm, coherently revealed by ionosonde, GNSS and LEO satellite data, is in agreement with what was observed by *Astafyeva et al.* [2020], who concluded that the PPEF were rather weak at this stage of the storm. The CEJ conditions drive the F-layer altitude drop and the vTEC and N_e decreases at LEO altitudes at the magnetic equator. The most intriguing features occur on 26 August, as the considered instruments simultaneously experience the superposition of CEJ conditions depleting **ExB** intensity with positive storm signatures at mid-latitude. The CEJ conditions result from the interplay of PPEF, identified by the strong oscillation of the IMF-B_z/IEF, and DDEF, linked with the J_h increase.

The equatorial region is featured by vTEC and N_e at LEO altitudes patterns that follow the CEJ conditions, with a single density peak at the magnetic equator, clearly depicted in correspondence of CSES-01 and Swarm A. Both ionosondes located at the dip-equator and the southern crest of the EIA observe an increase of f_oF2. For the equator station, this is due to the decrease of the eastward electric field, while for the crest station to the equatorward thermospheric winds induced

by the storm, as confirmed by the averaged neutral density measured by Swarm C that passes from about $3 \cdot 10^{-13}$ kg/m^3 on 24 August to about $9.5 \cdot 10^{-13}$ kg/m^3 on 26 August (not shown). This mechanism is further confirmed looking at the variations of f_oF2 over Bahia Blanca (Argentina, 38.7ºS; 62.3ºW), located at mid-latitude, that reveal the occurrence of a positive ionospheric storm due to the storm-induced equatorward thermospheric wind, particularly evident on 26 and 27 August (not shown). Indeed, a disturbance propagation from higher to lower latitudes associated to a positive ionospheric storm and vertical plasma drift enhancement is typically clearly seen in f_oF2 variations with a delayed reaction of the F2-layer at the stations located further from the origin of the thermosphere heating in the auroral zone [see, e.g., *Prölss*, 1995, 2004; *Balan, 2010; Mikhailov et al.*, 2012].

From 28 August onwards, the EEJ pattern presents an amplitude modulation of the quiet conditions. In the same period, *foF2* increases at the crest ionosonde station and a *foF2* decrease at equatorial station due to the increase of EEJ. The main controlling parameter of the day-to-day equatorial NmF2 variations is vertical ExB plasma drift, which in this case is upward. Clear signatures of the EIA crests are also recorded as per N_e latitudinal profile from LEO satellites and vTEC from the maps calculated along the LEO tracks. As the latitudinal profile of N_e is analyzed for both hemispheres, interhemispheric asymmetry is found and explained as due to both seasonality and different heating of the polar caps, being larger in the northern hemisphere. The comparison between N_e and vTEC along the LEO tracks allows also the EIA peaks to be tagged at poleward latitudes with respect to N_e peaks, because of the altitude-latitude variations of the electron density [*Balan et al.*, 2018]. Hence, EEJ and related ionospheric features in the late recovery (from 28 August onwards) are mainly due to the day-to-day variability, whose short-term variation is due to the irregular variability in the neutral winds. In addition, such EEJ variation has a periodicity of about 3.8 days, being compatible with planetary waves, reinforcing the idea the deviation from the regular behavior is also strictly related to tidal waves of lower atmospheric origin. [*Yamazaki & Maute*, 2017].

We also identified a further magnetospheric compression on 31 August in association with a PPEF event, which increased the EEJ and delayed its peak at the time of CSES-01 passage, allowing identifying the crest signatures at CSES-01 altitudes.

Acknowledgments and Data availability

References

Abdu, M. A. (1997). Major phenomena of the equatorial ionosphere-thermosphere system under disturbed conditions. Journal of Atmospheric and Solar-Terrestrial Physics, 59(13), 1505-1519.

Abdu, M. A., Batista, I. S., Carrasco, A. J., & Brum, C. G. M. (2005). South Atlantic magnetic anomaly ionization: A review and a new focus on electrodynamic effects in the equatorial ionosphere. Journal of Atmospheric and Solar-Terrestrial Physics, 67(17-18), 1643-1657.

Abdu, M. A., Kherani, E. A., Batista, I. S., & Sobral, J. H. A. (2009). Equatorial evening prereversal vertical drift and spread F suppression by disturbance penetration electric fields. Geophysical research letters, 36(19).

Afolayan, A. O., Mandeep, J. S., Abdullah, M., & Buhari, S. M. (2019). Observation of the north-south asymmetry in the equatorial spread F intensity at the Brazilian longitude. Advances in Space Research.

Akiyama, T., Yoshikawa, A., Fujimoto, A., & Uozumi, T. (2019). Relationship between plasma bubble and ionospheric current, equatorial electrojet, and equatorial counter electrojet. In Journal of Physics: Conference Series (Vol. 1152, No. 1, p. 012022). IOP Publishing.

Alfonsi, L., Spogli, L., Tong, J. R., De Franceschi, G., Romano, V., Bourdillon, A., ... & Mitchell, C. N. (2011). GPS scintillation and TEC gradients at equatorial latitudes in April 2006. Advances in space Research, 47(10), 1750-1757.

Astafyeva, E., Bagiya, M. S., Förster, M., & Nishitani, N. (2020). Unprecedented hemispheric asymmetries during a surprise ionospheric storm: a game of drivers. Journal of Geophysical Research: Space Physics, 125(3), e2019JA027261.

Balan, N., Shiokawa, K., Otsuka, Y., Kikuchi, T., Vijaya Lekshmi, D., Kawamura, S., ... & Bailey, G. J. (2010). A physical mechanism of positive ionospheric storms at low latitudes and midlatitudes. Journal of Geophysical Research: Space Physics, 115(A2).

Balan, N., Liu, L., & Le, H. (2018). A brief review of equatorial ionization anomaly and ionospheric irregularities. Earth and Planetary Physics, 2(4), 257-275.

Barlier, F., P. Bauer, C. Jaeck, G. Thuillier, and G. Kockarts (1974), North-South asymmetries in the thermosphere during the last maximum of the solar cycle, J. Geophys. Res., 79, 5273-5285.

Batista, I. S., Abdu, M. A., & Bittencourt, J. A. (1986). Equatorial F region vertical plasma drifts: Seasonal and longitudinal asymmetries in the American sector. Journal of Geophysical Research: Space Physics, 91(A11), 12055-12064.

Blanc, M., & Richmond, A. D. (1980). The ionospheric disturbance dynamo. Journal of Geophysical Research: Space Physics, 85(A4), 1669-1686.

Cardoso, F. A., Sahai, Y., Guarnieri, F. L., Fagundes, P. R., Pillat, V. G., & da Silva, J. V. P. R. (2011). Dependence of the F-region peak electron density (foF2) on solar activity observed in the equatorial ionospheric anomaly region in the Brazilian sector. Advances in space research, 48(5), 837-841.

Cesaroni, C., Spogli, L., Alfonsi, L., De Franceschi, G., Ciraolo, L., Monico, J. F. G., ... & Bougard, B. (2015). L-band scintillations and calibrated total electron content gradients over Brazil during the last solar maximum. Journal of Space Weather and Space Climate, 5, A36.

Chen, C., Liu, Y. D., Wang, R., Zhao, X., Hu, H., & Zhu, B. (2019). Characteristics of a gradual filament eruption and subsequent CME propagation in relation to a strong geomagnetic storm. The Astrophysical Journal, 884(1), 90.Z1

Ciraolo, L., Azpilicueta, F., Brunini, C., Meza, A., & Radicella, S. M. (2007). Calibration errors on experimental slant total electron content (TEC) determined with GPS. Journal of Geodesy, 81(2), 111-120.

Davies, K. (1990). Ionospheric radio (No. 31). IET.

Davies, K., & Liu, X. M. (1991). Ionospheric slab thickness in middle and low latitudes. Radio Science, 26(4), 997-1005.

Dudeney, J. R. (1983). The accuracy of simple methods for determining the height of the maximum electron concentration of the F2-layer from scaled ionospheric characteristics. Journal of atmospheric and terrestrial physics, 45(8-9), 629-640.

Elias, A. G., Zossi, B. S., Yiğit, E., Saavedra, Z., & de Haro Barbas, B. F. (2017). Earth's magnetic field effect on MUF calculation and consequences for hmF2 trend estimates. Journal of Atmospheric and Solar-Terrestrial Physics, 163, 114-119.

Fejer, B. G. (1991). Low latitude electrodynamic plasma drifts: A review. Journal of Atmospheric and Terrestrial Physics, 53(8), 677-693.

Fejer, B. G., Souza, J. R., Santos, A. S., & Costa Pereira, A. E. (2005). Climatology of F region zonal plasma drifts over Jicamarca. Journal of Geophysical Research: Space Physics, 110(A12).

Fejer, B. G. (2011). Low latitude ionospheric electrodynamics. Space Science Reviews, 158(1), 145-166.

Fejer, B. G., Blanc, M., & Richmond, A. D. (2017). Post-storm middle and low-latitude ionospheric electric fields effects. Space Science Reviews, 206(1-4), 407-429.

Friis-Christensen, E., H. Lühr, D. Knudsen, and R. Haagmans (2008), Swarm—An Earth observation mission investigating geospace, Adv. Space Res., 41(1), 210–216.

Fuller-Rowell, T. J., Millward, G. H., Richmond, A. D., & Codrescu, M. V. (2002). Storm-time changes in the upper atmosphere at low latitudes. Journal of atmospheric and solar-terrestrial physics, 64(12-14), 1383-1391.

Kelley, M. C. (2009). The Earth's ionosphere: plasma physics and electrodynamics. Academic press.

Khadka, S. M., Valladares, C. E., Sheehan, R., & Gerrard, A. J. (2018). Effects of electric field and neutral wind on the asymmetry of equatorial ionization anomaly. Radio Science, 53(5), 683-697.

King, J. H., & Papitashvili, N. E. (2005). Solar wind spatial scales in and comparisons of hourly Wind and ACE plasma and magnetic field data. Journal of Geophysical Research: Space Physics, 110(A2).

Kintner, P. M., Humphreys, T. E., & Hinksn, J. (2009). GNSS and Ionospheric Scintillation: How to survive the next solar maximum. InsideGNSS 22-30.

Laken, B. A., & Čalogović, J. (2013). Composite analysis with Monte Carlo methods: an example with cosmic rays and clouds. Journal of Space Weather and Space Climate, 3, A29.

Li, H., Wang, C., & Kan, J. R. (2011). Contribution of the partial ring current to the SYMH index during magnetic storms. Journal of Geophysical Research: Space Physics, 116(A11).

Mannucci, A. J., Wilson, B. D., Yuan, D. N., Ho, C. H., Lindqwister, U. J., & Runge, T. F. (1998). A global mapping technique for GPS-derived ionospheric total electron content measurements. Radio science, 33(3), 565-582.

Manoj, C., & Maus, S. (2012). A real-time forecast service for the ionospheric equatorial zonal electric field. Space Weather, 10(9).

Manoj, C., Maus, S., & Alken, P. (2013). Long-period prompt-penetration electric fields derived from CHAMP satellite magnetic measurements. Journal of Geophysical Research: Space Physics, 118(9), 5919-5930.

Manoj, C., Maus, S., Lühr, H., & Alken, P. (2008). Penetration characteristics of the interplanetary electric field to the daytime equatorial ionosphere. Journal of Geophysical Research: Space Physics, 113(A12).

Manoj, C., Lühr, H., Maus, S., and Nagarajan, N. (2006), Evidence for short spatial correlation lengths of the noontime equatorial electrojet inferred from a comparison of satellite and ground magnetic data, J. Geophys. Res., 111, A11312.

MacDougall, J. W. (1969). The equatorial ionospheric anomaly and the equatorial electrojet. Radio Science, 4(9), 805-810.

McNamara, L. F. (2008). Accuracy of models of hmF2 used for long-term trend analyses. Radio Science, 43(02), 1-12.

Mendillo, M. (2006). Storms in the ionosphere: Patterns and processes for total electron content. Reviews of Geophysics, 44(4).

Mikhailov, A. V., Perrone, L., & Smirnova, N. V. (2012). Two types of positive disturbances in the daytime mid-latitude F2-layer: Morphology and formation mechanisms. Journal of atmospheric and solar-terrestrial physics, 81, 59-75.

Morschhauser, A., Brando Soares, G., Haseloff, J., Bronkalla, O., Protásio, J., Pinheiro, K., and Matzka, J. (2017), The magnetic observatory on Tatuoca, Belém, Brazil: history and recent

developments, Geosci. Instrum. Method. Data Syst., 6, 367–376, https://doi.org/10.5194/gi-6-367-2017.

Muella, M. T. A. H., E. A. Kherani, E. R. de Paula, A. P. Cerruti, P. M. Kintner, I. J. Kantor, C. N. Mitchell, I. S. Batista, and M. A. Abdu (2010), Scintillation-producing Fresnel-scale irregularities associated with the regions of steepest TEC gradients adjacent to the equatorial ionization anomaly, J. Geophys. Res., 115, A03301, doi:10.1029/2009JA014788.

Muella, M. T., Duarte-Silva, M. H., Moraes, A. O., de Paula, E. R., de Rezende, L. F., Alfonsi, L., & Affonso, B. J. (2017). Climatology and modeling of ionospheric scintillations and irregularity zonal drifts at the equatorial anomaly crest region. Ann. Geophys, 35, 1201-1218.

Nishida A. 1968. Coherence of geomagnetic DP 2 fluctuations with interplanetary magnetic variations. J Geophys Res 73(17): 5549–5559.

Pi, X., Mannucci, A. J., Lindqwister, U. J., & Ho, C. M. (1997). Monitoring of global ionospheric irregularities using the worldwide GPS network. Geophysical Research Letters, 24(18), 2283-2286.

Perrone, L., Mikhailov, A., Cesaroni, C., Alfonsi, L., De Santis, A., Pezzopane, M., & Scotto, C. (2017). Long-term variations of the upper atmosphere parameters on Rome ionosonde observations and their interpretation. Journal of Space Weather and Space Climate, 7, A21.

Pezzopane, M. (2004). Interpre: a Windows software for semiautomatic scaling of ionospheric parameters from ionograms. Computers & Geosciences, 30(1), 125-130.

Piersanti, M., De Michelis, P., Del Moro, D., Tozzi, R., Pezzopane, M., Consolini, G., ... & Quattrociocchi, V. (2020). From the Sun to the Earth: August 25, 2018 geomagnetic storm effects. Annales Geophysicae Discussions, 1-30.

Piggott, W. R., & Rawer, K. (1972). URSI handbook of ionogram interpretation and reduction, Rep. UAG-23,, 15.

Pokhotelov, D., Mitchell, C. N., Jayachandran, P. T., MacDougall, J. W., & Denton, M. H. (2009). Ionospheric response to the corotating interaction region–driven geomagnetic storm of October 2002. Journal of Geophysical Research: Space Physics, 114(A12).

Prölss, G. W. (1995). Ionospheric F region storms. Handbook of Atmospheric Electrodynamics, 195-248.

Prölss, G.W. (2004). Physics of the Earth's Space Environment – An Introduction, Springer-Verlag Berlin Heidelberg.

Rastogi, R. G. (2007). Day-to-day variability of the equatorial electrojet current in the South American sector. Earth, planets and space, 59(5), 459-461.

Rastogi, R. G., and Klobuchar, J. A. (1990), Ionospheric electron content within the equatorial F2-layer anomaly belt, J. Geophys. Res., 95(A11), 19045– 19052, doi:10.1029/JA095iA11p19045.

Regi, M., Redaelli, G., Francia, P., & De Lauretis, M. (2017). ULF geomagnetic activity effects on tropospheric temperature, specific humidity, and cloud cover in Antarctica, during 2003–2010. Journal of Geophysical Research: Atmospheres, 122(12), 6488-6501.

Rishbeth, H. & Garriott, O. (1969). Introduction to ionospheric physics, Academic Press.

Rishbeth, H. (1971). Polarization fields produced by winds in the equatorial F-region. Planetary and Space Science, 19(3), 357-369.

Scherliess, L., & Fejer, B. G. (1997). Storm time dependence of equatorial disturbance dynamo zonal electric fields. Journal of Geophysical Research: Space Physics, 102(A11), 24037-24046.

Scotto, C., & Pezzopane, M. A software for automatic scaling of foF2 and MUF (3000) F2 from ionograms. In Proceedings of the URSI XXVIIth General Assembly, Maastricht, Holland, 17–24 August 2002.

Scotto, C. (2009). Electron density profile calculation technique for Autoscala ionogram analysis. Adv. Space Res., 44, 756–766.

Scotto, C., & Sabbagh, D. (2020). The Accuracy of Real-Time hmF2 Estimation from Ionosondes. Remote Sens., 12(17), 2671. https://doi.org/10.3390/rs12172671.

Shen, X. H., Zhang, X. M., Yuan, S. G., Wang, L. W., Cao, J. B., Huang, J. P., Zhu, X. H., Piergiorgio, P., and Dai, J. P. (2018). The state-of-the-art of the China Seismo-Electromagnetic Satellite mission. Sci. China Technol. Sci., 61(5), 634–642. https://doi.org/10.1007/s11431-018-9242-0

Shimazaki, T., (1955). World daily variability in the height of the maximum electron density of the ionospheric F2-layer. J. Radio Res. Lab. (Jpn.) 2, 85–97.

Smith, C. W., L'Heureux, J., Ness, N. F., Acuna, M. H., Burlaga, L. F., & Scheifele, J. (1998). The ACE magnetic fields experiment. In The advanced composition explorer mission (pp. 613-632). Springer, Dordrecht.

Smith, J. O. (2007), Introduction to Digital Filters with Audio Applications, online book, Stanford University, Stanford, Calif. (Available at https://ccrma.stanford.edu/~jos/filters/)

Soares, G. B., Yamazaki, Y., Matzka, J., Pinheiro, K., Morschhauser, A., Stolle, C., Alken, P. (2018), Equatorial Counter Electrojet Longitudinal and Seasonal Variability in the American Sector. - Journal of Geophysical Research, 123, 11, pp. 9906—9920.

Spogli, L., Alfonsi, L., Romano, V., De Franceschi, G., Francisco, G. M. J., Shimabukuro, M. H., ... & Aquino, M. (2013). Assessing the GNSS scintillation climate over Brazil under increasing solar activity. Journal of Atmospheric and Solar-Terrestrial Physics, 105, 199-206.

Spogli, L., Cesaroni, C., Di Mauro, D., Pezzopane, M., Alfonsi, L., Musicò, E., ... & Linty, N. (2016). Formation of ionospheric irregularities over Southeast Asia during the 2015 St. Patrick's Day storm. Journal of Geophysical Research: Space Physics, 121(12), 12-211.

Tulasi Ram, S., Su, S. Y., & Liu, C. H. (2009). FORMOSAT-3/COSMIC observations of seasonal and longitudinal variations of equatorial ionization anomaly and its interhemispheric asymmetry during the solar minimum period. Journal of Geophysical Research: Space Physics, 114(A6).

Vani, B. C., Shimabukuro, M. H., & Monico, J. F. G. (2017). Visual exploration and analysis of ionospheric scintillation monitoring data: the ISMR query tool. Computers & Geosciences, 104, 125-134.

Vanlommel, P. (2018) Solar-Terrestrial Centre of Excellence (STCE) Newsletter, 20-26 Aug 2018, http://www.stce.be/newsletter/pdf/2018/STCEnews20180831.pdf

Venkatesh, K., Fagundes, P. R., Prasad, D. V., Denardini, C. M., De Abreu, A. J., De Jesus, R., & Gende, M. (2015). Day-to-day variability of equatorial electrojet and its role on the day-to-day characteristics of the equatorial ionization anomaly over the Indian and Brazilian sectors. Journal of Geophysical Research: Space Physics, 120(10), 9117-9131.

Venkatesh, K., Tulasi Ram, S., Fagundes, P. R., Seemala, G. K., & Batista, I. S. (2017). Electrodynamic disturbances in the Brazilian equatorial and low-latitude ionosphere on St. Patrick's Day storm of 17 March 2015. Journal of Geophysical Research: Space Physics, 122(4), 4553-4570.

Villante, U., & Regi, M. (2008). Solar flare effect preceding Halloween storm (28 October 2003): Results of a worldwide analysis. Journal of Geophysical Research: Space Physics, 113(A3).

Wei, Y., Zhao, B., Li, G., & Wan, W. (2015). Electric field penetration into Earth's ionosphere: A brief review for 2000–2013. Science Bulletin, 60(8), 748-761.

Weimer, D. R. (2005a). Improved ionospheric electrodynamic models and application to calculating Joule heating rates. Journal of Geophysical Research: Space Physics, 110(A5).

Weimer, D. R. (2005b). Predicting surface geomagnetic variations using ionospheric electrodynamic models. Journal of Geophysical Research: Space Physics, 110(A12).

Weimer, D. R., Edwards, T. R., & Olsen, N. (2017). Linear response of field-aligned currents to the interplanetary electric field. Journal of Geophysical Research: Space Physics, 122(8), 8502-8515.

Xiong, C., Lühr, H., & Ma, S. Y. (2013). The magnitude and inter-hemispheric asymmetry of equatorial ionization anomaly-based on CHAMP and GRACE observations. Journal of Atmospheric and Solar-Terrestrial Physics, 105, 160-169.

Yamazaki, Y., & Maute, A. (2017). Sq and EEJ—A review on the daily variation of the geomagnetic field caused by ionospheric dynamo currents. Space Science Reviews, 206(1-4), 299-405.

Yan, R., Guan, Y., Shen, X., Huang, J., Zhang, X., Liu, C., & Liu, D. (2018). The Langmuir Probe onboard CSES: data inversion analysis method and first results. Earth and Planetary Physics, 2(6), 479-488.

Yang, Y. Y., Zhima, Z. R., Shen, X. H., Chu, W., Huang, J. P., Wang, Q., ... & Liu, D. P. (2020). The First Intense Geomagnetic Storm Event Recorded by the China Seismo-Electromagnetic Satellite. Space Weather, 18(1), e2019SW002243.

Table 1. Mean geographic Local Time and time range (in UT) of the selected tracks.

Day of August 2018	Swarm A		CSES-01	
	LT	UT	LT	UT
10 (ref. quiet)	15:22	19:23/19:34	14:02	16:45/16:54
24	14:40	17:58/18:10	14:02	17:02/17:14
25	14:35	17:19/17:30	14:02	16:43:16:54
26	14:29	16:39/16:51	14:02	17:59/18:11
27	14:24	17:33/17:45	14:02	17:40/17:52
28	14:19	16:54/17:05	14:02	17:21/17:33
29	14:13	16:14/16:26	14:02	17:02/17:14
30	14:08	17:08/17:20	14:02	16:43/16:55
31	14:03	16:29/16:40	14:02	16:24/16:36

Table 2. Geodetic and magnetic dipole coordinates of the geomagnetic observatories computed from IGRF-13th generation at epoch 2018.6.

IAGA	Latitude (°N)	Longitude (°E)	Mlat (°N)	Mlon (°E)
KOU	5.21	307.27	14.10	24.49
TTB	-1.21	311.49	7.51	20.36
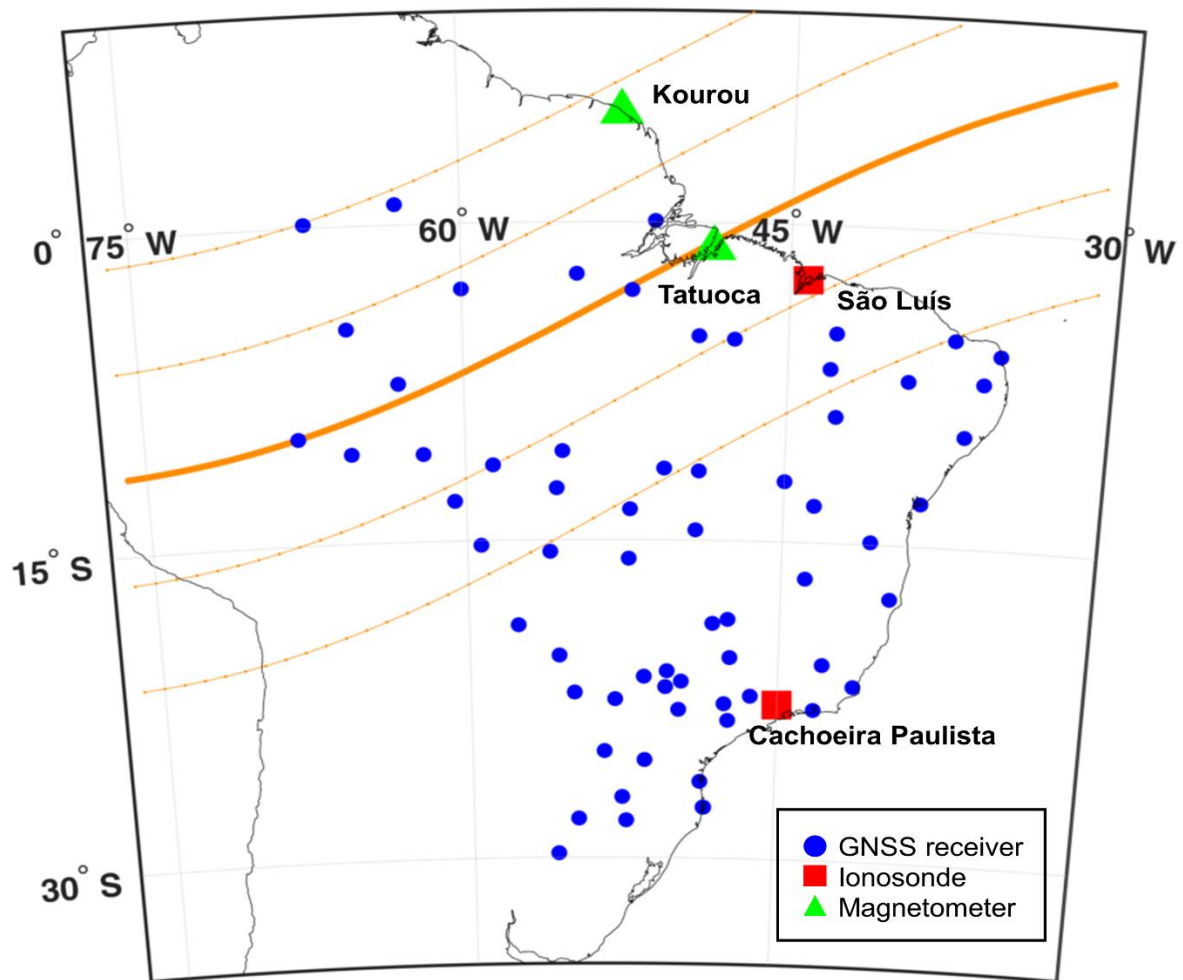
Figure 1. Location of the ground-based instruments. The orange thick line represents the position of the magnetic equator, while orange thin lines represent the isoclinic lines at magnetic latitudes equal to ±5° and ±10°.
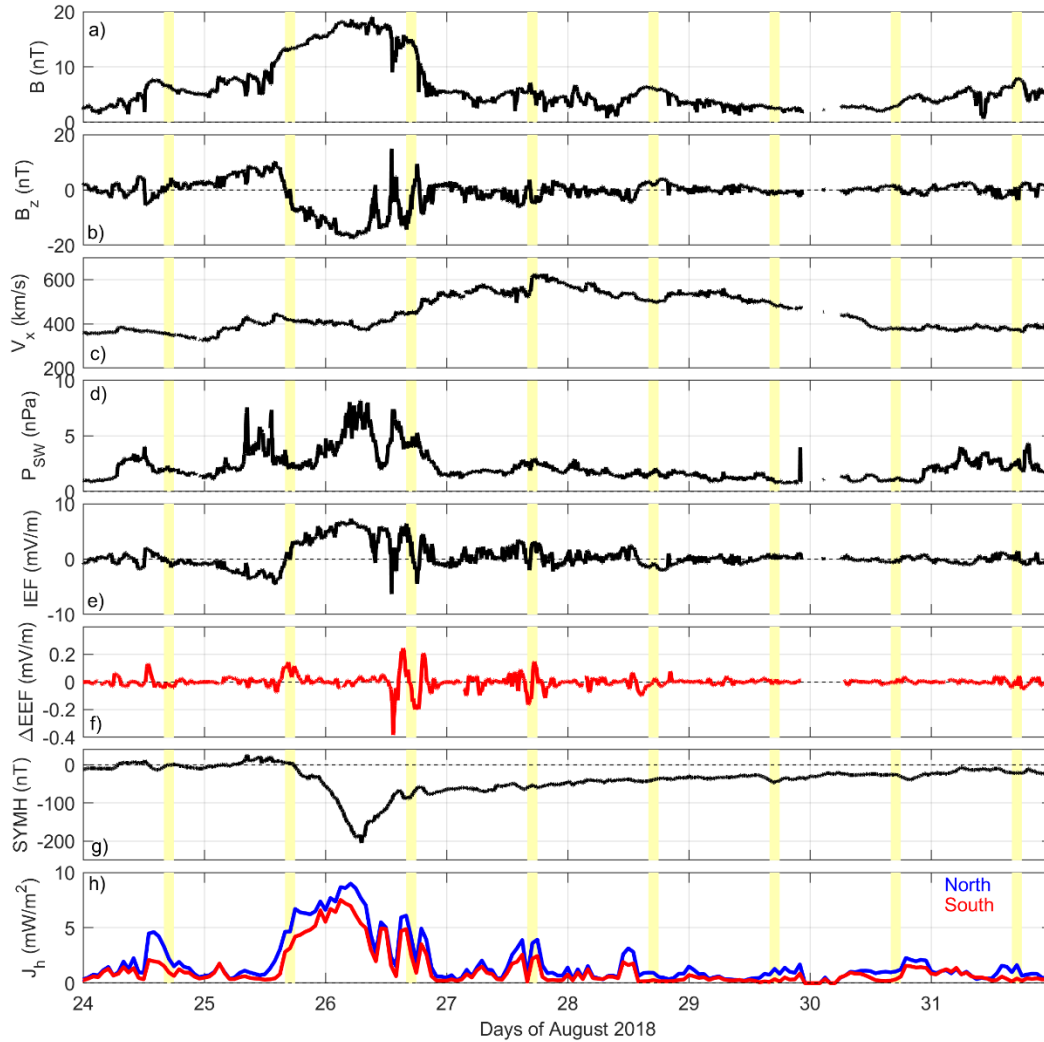
Figure 2. Time series of the total intensity of the Interplanetary Magnetic Field (B) (panel a), of its z-component (B$_z$) (panel b), of the radial component of the solar wind velocity (panel c), of the solar wind pressure (panel d), of the Interplanetary Electric Field (panel e), of the disturbance to the Equatorial Electric Field adjusted for the local time (panel f), of the SYMH index (panel g) and of the Joule heating (J$_h$) estimated for the northern (blue) and southern (red) polar caps (panel h). The yellow vertical areas indicate the time range between 16:00 UT and 18:00 UT.
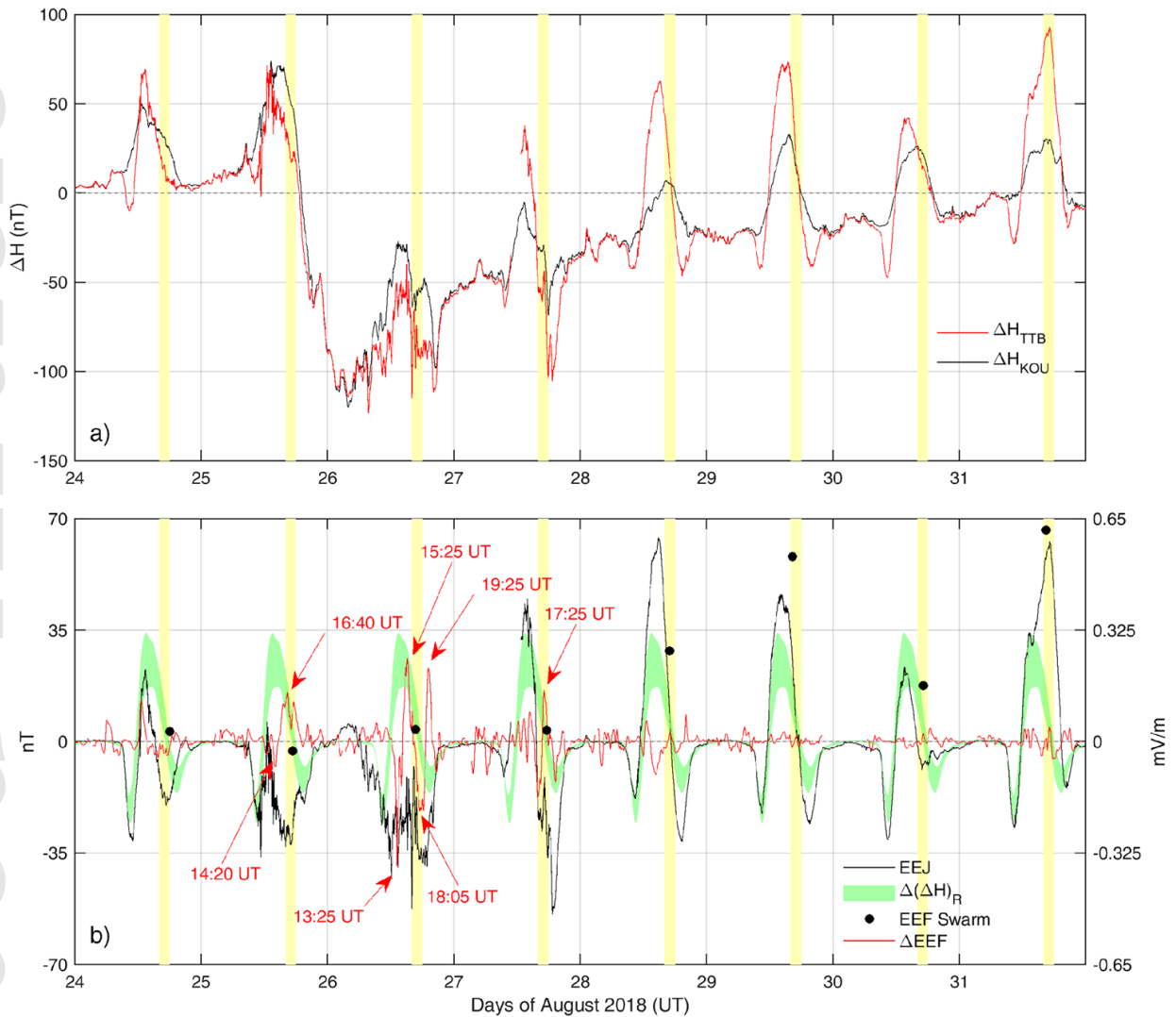
Figure 3. (Panel a): time series of *ΔH* at TTB (red) and KOU (black). Bottom panel: time series of the difference EEJ = *Δ(ΔH)* = *ΔH_{TTB}* - *ΔH_{KOU}* (black line), of *ΔEEF* (red, same as in Figure 2) and of the EEF measured by Swarm A (black dots). The green strip represents the reference difference for solar quiet conditions *Δ(ΔH)_R* (average over days with daily Kp<1) with confidence level of 1%. The yellow vertical areas indicate the time range between 16:00 UT and 18:00 UT. The red arrows and text indicate the time of *ΔEEF* main peaks.
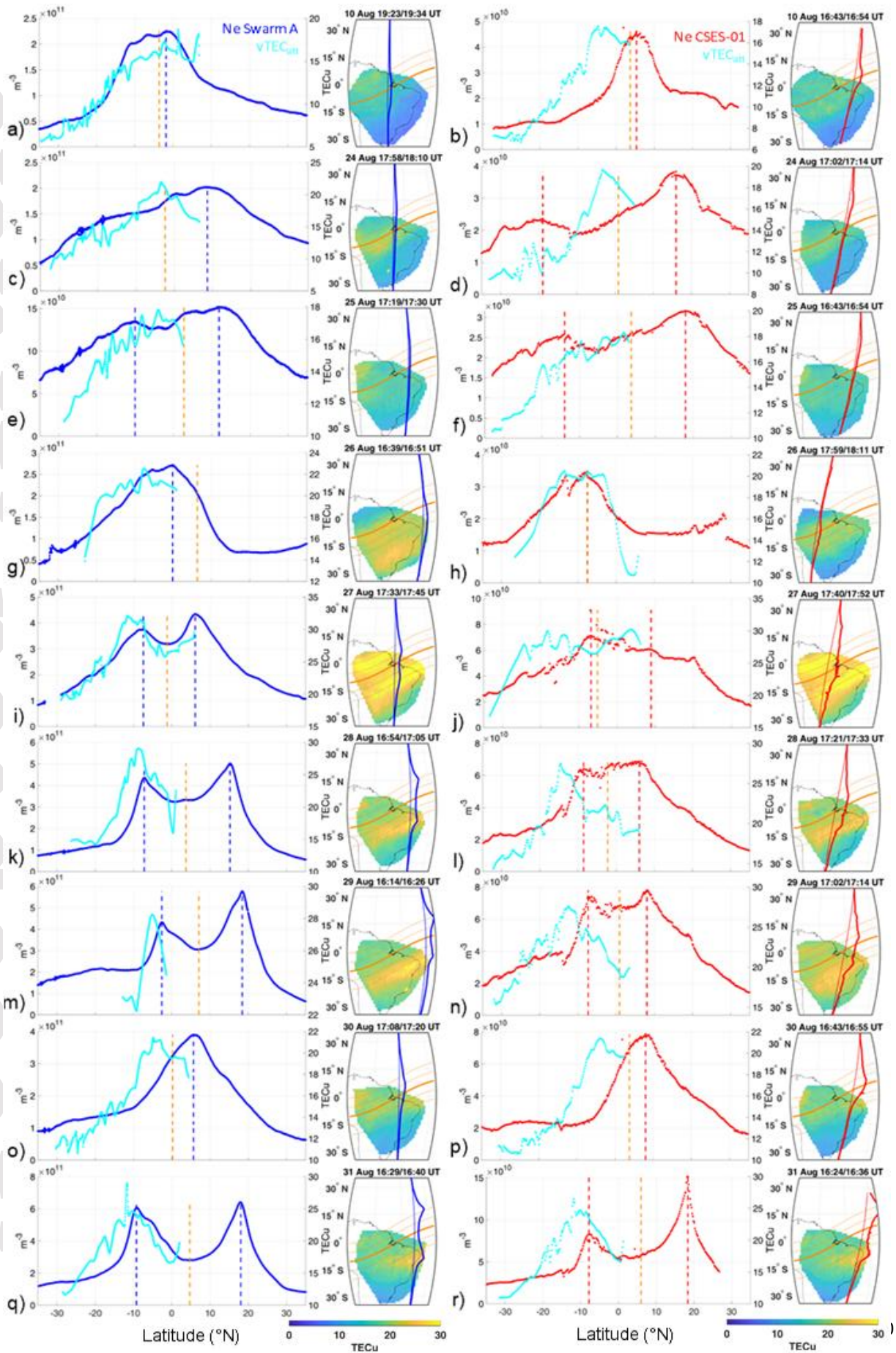
Figure 4. (Left plot of each panel) *In situ* **electron density as measured by Swarm A (blue) and CSES-01 (red) satellites whose relative maxima are indicated with a vertical dashed line, according to the same color code. The orange vertical dashed line indicates the latitude of the magnetic equator at the track crossing. The value of the $vTEC_{att}$ is reported in cyan. (Right plot of each panel). Maps of vTEC obtained by integrating TEC measurements covering the time interval of the satellites passages (see Table 1). Blue and red thick lines indicate the** *in situ* **electron density of Swarm-A and CSES-01, respectively. The larger the longitudinal positive deviation from the ground track, the larger the electron density. Orange thick line represents the position of the magnetic equator, while orange thin lines represent the isoclinic lines at magnetic latitudes equal to ±5° and ±10°.**
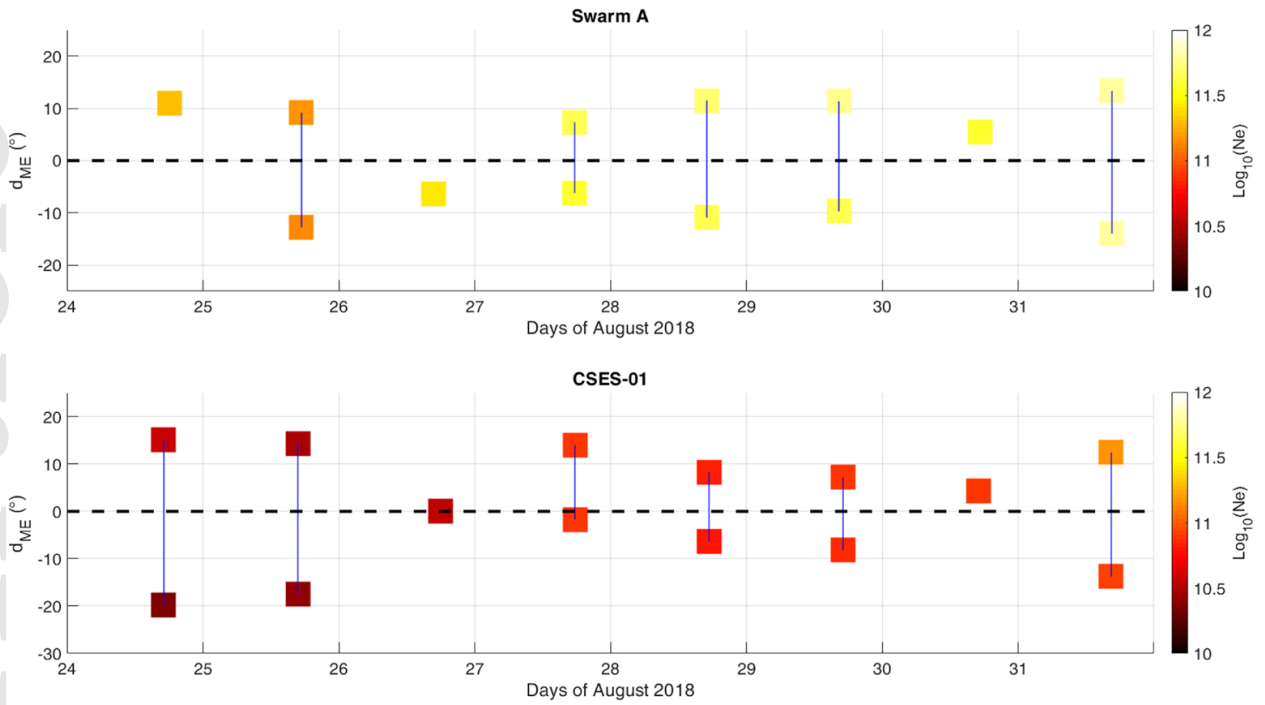
Figure 5. Distance from magnetic equator of the electron density maximum/maxima for Swarm A (top plot) and CSES-01 (bottom plot) satellites. The corresponding electron density is indicated in color code.
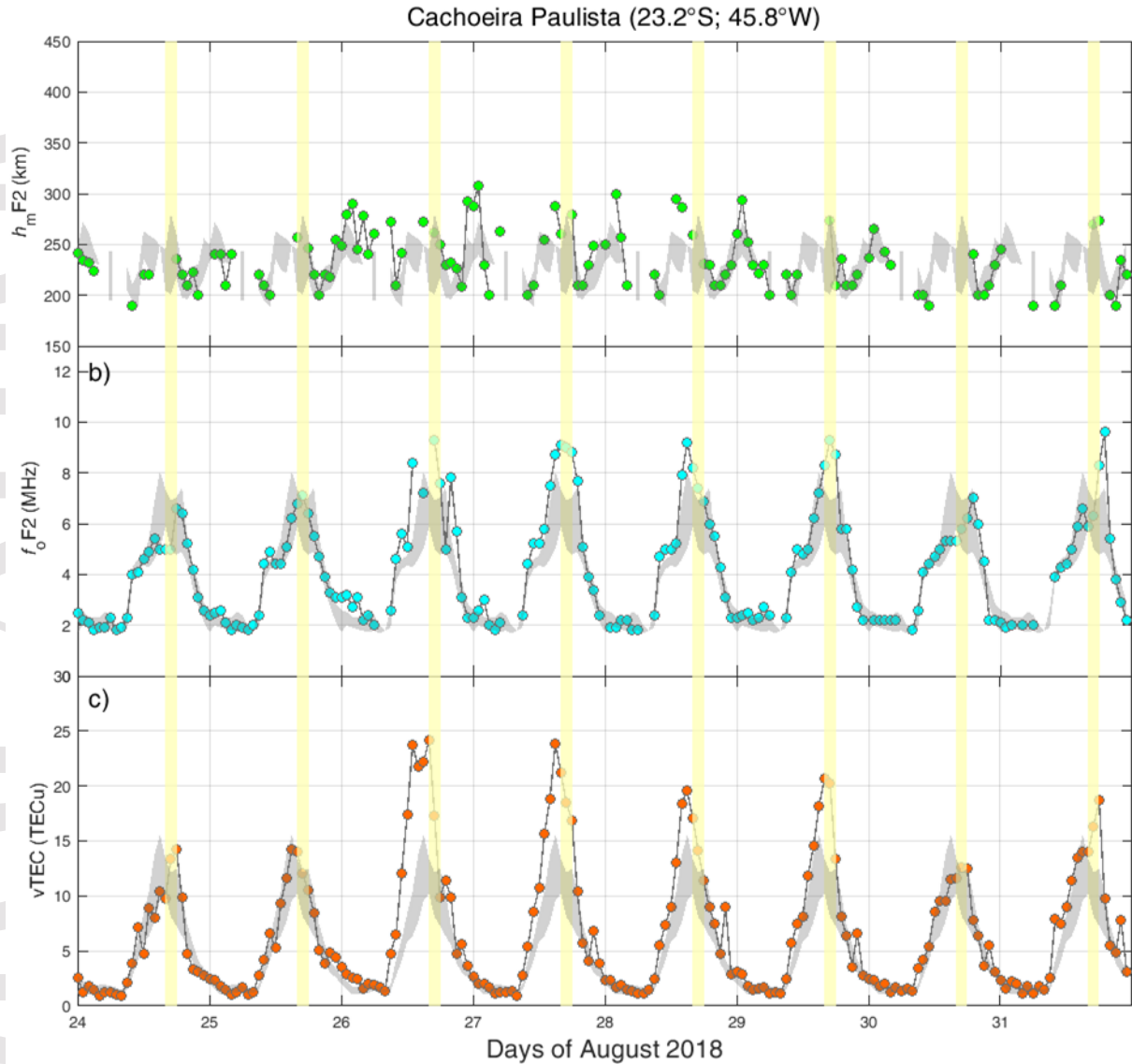
Figure 6. Time series of the hourly values of h_{m}F2 (green, panel a), f_{o}F2 (cyan, panel b), and vTEC (orange, panel c) over Cachoeira Paulista. Gray shaded areas represent the ±1 σ band around the mean value for the quiet reference (days with daily Kp<1 in the range 08 August to 09 September 2018). Yellow-shaded boxes indicate the intervals between 16:00 and 18:00 UT.
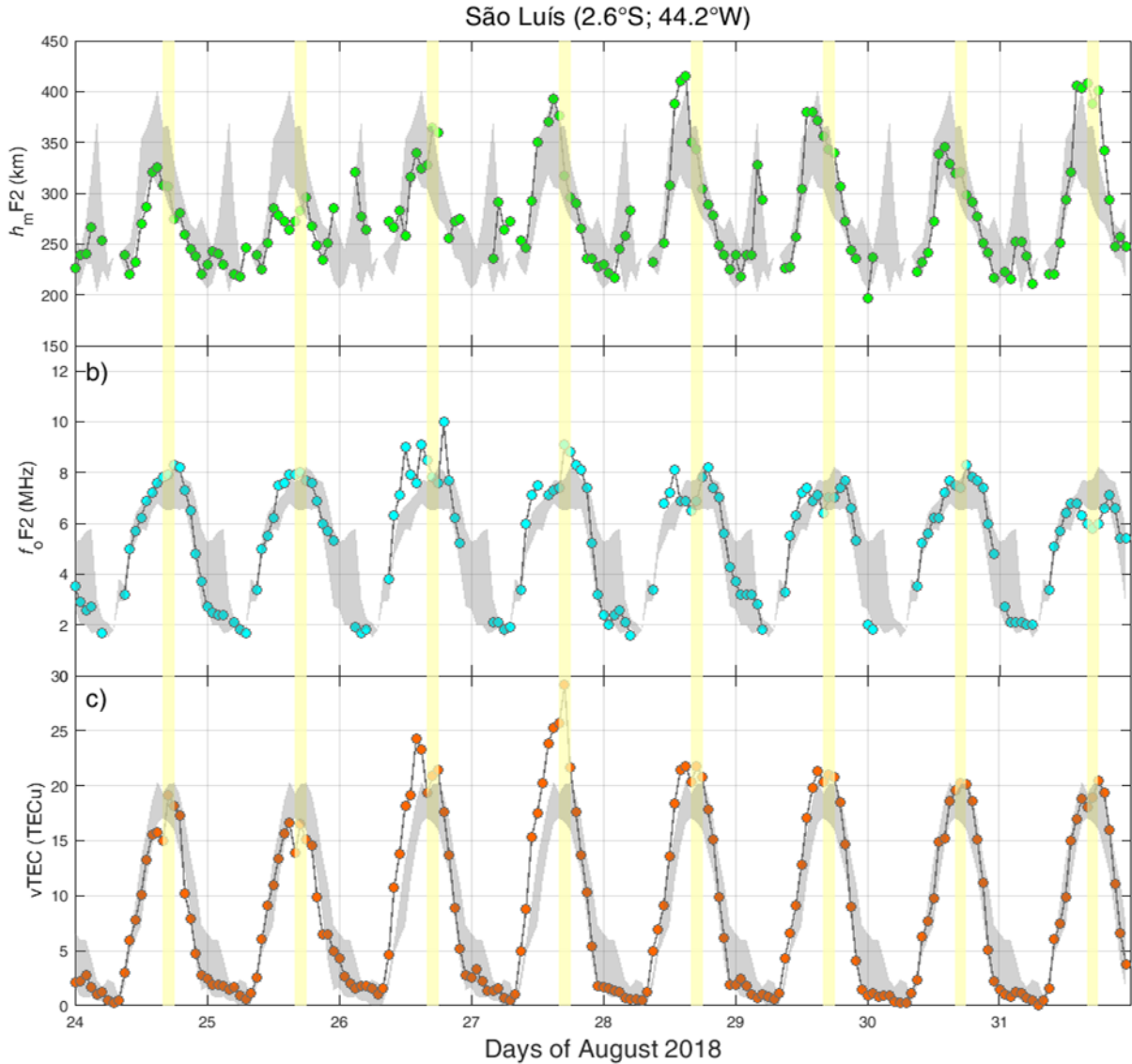
Figure 7. Time series of the hourly values of h_mF2 (green, panel a), f_oF2 (cyan, panel b), and vTEC (orange, panel c) over São Luís. Gray shaded areas represent the ±1 σ band around the mean value for the quiet reference (days with daily Kp<1 in the range 08 August to 09 September 2018). Yellow-shaded boxes indicate the intervals between 16:00 and 18:00 UT.